Aerospace Science and Technology 168 (2026) 111067

Contents lists available at ScienceDirect

Aerospace Science and Technology

journal homepage: www.elsevier.com/locate/aescte

Advanced shape sensing of a full-scale composite UAV stabilizer under non-ideal boundary conditions using the inverse finite element method

Jacopo Bardiani *, Dario Poloni, Daniele Oboe, Marco Giglio, Andrea Manes, Claudio Sbarufatti

Politecnico di Milano, Department of Mechanical Engineering, Via G. La Masa 1, Milano 20156, Italy

ARTICLE INFO

Edited by Dr. Duc Dinh Nguyen

Keywords:
Non-ideal boundary conditions
Shape sensing
Inverse finite element method
Distributed fiber optic
Structural health monitoring
UAV stabilizer

ABSTRACT

The inverse Finite Element Method (iFEM) is a robust and efficient computational technique for reconstructing full-field displacements from strain measurements, requiring only structural geometry, boundary conditions, and sensor data—without the need for material properties or external load information. While its independence from loading conditions makes it particularly suitable for aerospace Structural Health Monitoring (SHM) and Digital Twin (DT) frameworks, three major challenges limit its application to aerospace composite structures: (i) most existing studies focus on simplified structural configurations rather than realistic, full-scale assemblies, (ii) sparse sensor layouts, which reduce reconstruction accuracy, and (iii) uncertainty or degradation of boundary conditions, which can significantly compromise shape sensing performance. This study presents a novel combined numerical–experimental methodology for advanced shape sensing of a full-scale composite Unmanned Aerial Vehicle (UAV) stabilizer under non-ideal boundary conditions. The approach integrates Smoothing Element Analysis (SEA) into the iFEM framework to pre-extrapolate strain fields from limited sensor measurements. Given the structural complexity of the stabilizer, SEA is applied on different planes of the structure, starting from instrumented areas and progressively extending to non-instrumented regions. Furthermore, the methodology explicitly accounts for non-ideal boundary constraints arising from joint loosening and support compliance. The methodology is experimentally validated on a full-scale composite stabilizer equipped with a LUNA distributed fiber optic sensor network, with reconstruction accuracy assessed under various ideal and non-ideal support configurations. Several experimental tests are performed in which the stabilizer is subjected to two external forces, inducing bending and torsion in a cantilever beam configuration. Results show that, when only ideal boundary conditions are assumed, displacement reconstruction errors can exceed 14 % at key measurement points, which is not acceptable for SHM purposes. By explicitly modeling joint loosening and support compliance, reconstruction errors are reduced to approximately 2 %, achieving the accuracy required for real-world applications. These findings highlight the potential of the proposed SEA–iFEM approach for real-time monitoring of complex composite aircraft structures in realistic operational scenarios, where non-ideal boundary conditions cannot be neglected.

1. Introduction

Ensuring structural integrity and accurately assessing potential damage are fundamental aspects for maintaining the safety and reliability of a wide range of structures and systems. The specific safety requirements vary depending on the intended application and are typically established based on the severity of the potential consequences associated with structural failure or malfunction. In this context, aeronautical structures represent one of the most safety-critical domains, as even minor failures can lead to catastrophic outcomes, posing significant risks to both human life and mission success [1,2]. Due to their anisotropic and layered nature, aeronautical composite structures are particularly susceptible to barely visible impact damage and internal delamination, which may compromise structural performance without clear external signs. This makes it essential to implement appropriate methods for inspecting and monitoring structural conditions over time.

For this reason, non-destructive testing (NDT) techniques—such as visual inspections, liquid penetrant testing, radiography, and magnetic

---

* Corresponding author.
E-mail address: jacopo.bardiani@polimi.it (J. Bardiani).

https://doi.org/10.1016/j.ast.2025.111067
Received 12 August 2025; Received in revised form 27 September 2025; Accepted 9 October 2025

particle inspection—are routinely carried out at scheduled maintenance intervals to identify the onset of damage at an early stage. While effective, these techniques often necessitate taking the aircraft out of service, resulting in operational downtime and significant economic implications for the overall maintenance and lifecycle management of the aircraft fleet. Moreover, when dealing with composite structures, traditional NDT methods may face challenges in detecting internal flaws such as delamination or matrix cracking, which often develop without clear external signs.

This issue can be partially addressed through the implementation of Structural Health Monitoring (SHM) and Prognostic Health Monitoring (PHM) systems, which are designed to enable real-time evaluation of the structural state. These systems rely on a network of permanently installed sensors capable of capturing the operational and environmental conditions experienced by the aircraft during service. In composite structures, where damage can develop internally without visible manifestations, SHM systems are particularly valuable for providing early insight into the onset and evolution of structural degradation. The collected data are then processed using either data-driven approaches [3–5] or model-based algorithms [6,7], which can detect anomalies and early signs of damage. By providing continuous monitoring and timely diagnostics, these techniques can extend the interval between scheduled maintenance operations, thereby reducing downtime and lowering the overall maintenance costs throughout the aircraft's lifecycle.

Data-driven algorithms typically leverage large sets of historical data to identify patterns and detect anomalies, whereas model-based approaches rely on accurate representations of the structure in both its undamaged and damaged states. In practice, many of these algorithms incorporate machine learning techniques—such as artificial neural networks (ANNs)—trained on databases containing various predefined damage scenarios to perform structural assessment tasks [8]. However, a major limitation shared by many SHM techniques in the literature is their strong dependency on the external loads acting on the structure [9]. This sensitivity to loading conditions reduces their robustness, especially in real-world applications—such as aircraft structures—-where external loads are often uncertain, variable, or difficult to measure. As a result, there is a growing interest in alternative methods capable of reconstructing the structural response independently of the external loading, using only measurable quantities such as strains.

In recent years, structural monitoring has undergone a significant paradigm shift with the emergence of the Digital Twin (DT) approach [10–13]. A DT is an integrated, multi-physics, multi-scale, and probabilistic simulation of a physical system, continuously updated using high-fidelity physical models, sensor data, fleet history, and other sources to accurately mirror the behavior and evolution of its real-world counterpart throughout its lifecycle [14]. Each physical aeronautical structure can be associated with a DT—a digital replica built through detailed and accurate modeling. The number of DT-related studies has grown rapidly, with applications spanning the aerospace sector [14–18], marine engineering (e.g., offshore wind turbines and naval transport) [19–21], and manufacturing processes [22–24]. In aerospace, DTs are currently used primarily for modeling aircraft airframes [15,16,18] and predicting the fatigue life of cracked or aging components [20,25]. Although there is no universally accepted definition of the DT architecture [11], most implementations share three core components: (i) the physical structure or system, (ii) its digital counterpart (also called the master model), and (iii) a connection between the physical and digital systems, typically enabled through a network of sensors, often referred to as the digital shadow. To be effective, a Digital Twin must run in real time, using sensor or simulated data to predict future structural states. This requires fast and accurate models, often based on ANNs, analytical methods, or surrogate models. Critically, for full-scale composite components, the DT must accurately replicate the current structural condition—including any damage—by incorporating real-time deformation and strain data. This capability enables near real-time structural assessment and supports damage diagnosis and prognosis within an SHM framework.

Among the various algorithms proposed in the literature, the inverse Finite Element Method (iFEM) stands out as a model-based technique capable of reconstructing the displacement field of a structure from strain measurements. Its implementation only requires a mesh discretization and boundary conditions, without the need for material properties or knowledge of external loads. The sole input consists of strain data acquired from sensors, making iFEM particularly efficient and suitable for real-time applications [2,26]. Typically, iFEM relies on strain sensors (such as strain gauges or fiber optic sensors) bonded to the outer surfaces of the structure, although some studies have explored the use of embedded sensors in composite materials [27]. Thanks to its independence from loading conditions and minimal modeling assumptions, iFEM is particularly well-suited for Digital Twin frameworks targeting the monitoring of full-scale composite structures in operational environments, such as those encountered in the aeronautical sector.

The iFEM was originally developed by A. Tessler et al. [28,29], and its formulation has since been extended to both beam structures [30–37] and shell structures [38–45]. The method is founded on the minimization of a least-squares functional that quantifies the error between strain measurements acquired from sensors and their numerical counterpart, expressed in terms of unknown nodal degrees of freedom [46,47]. Various inverse finite elements have been developed to support shape sensing and structural health monitoring applications. Notable shell elements, such as iMIN3 (three-node flat shell element based on Mindlin theory, [48,49]), iQS4 (inverse Quadrilateral Shell element with 4 nodes, [41,50,51]), and iCS8 (inverse Curved Shell element with 8 nodes, [52]), employ first-order shear deformation theory with C0-continuous interpolation functions. A comparative study has evaluated the performance of these elements under various application scenarios [53]. Among these, iQS4 element has garnered significant attention due to its effectiveness in modeling large-scale systems with low-cost sensor networks and its ability to provide highly accurate displacement predictions. The iQS4 element has been widely applied to ships such as container ships [2,39], bulk carriers [54], chemical tankers [38], offshore platforms [51], and aerospace structures [43,55,56].

The versatility of iFEM is further demonstrated by its successful application to multilayered and sandwich composite structures, where it has been employed for displacement and stress monitoring under varying load conditions. Refined theoretical formulations have recently been integrated into the iFEM framework to capture zigzag deformations across the thickness of sandwich plates and beams [57–59], with validation provided by both numerical and experimental studies on moderately thick panels, especially in the context of aerospace structures [60]. Experimental implementations have demonstrated practicality for real-time shape and strain sensing in composite panels, including those subjected to impact damage or complex boundary conditions [61,62]. Moreover, the iFEM methodology has been applied to complex scenarios such as the detection of delamination damage in composite structures [63,64] and real-time crack propagation monitoring in fiber-reinforced composites [65]. These developments emphasize the versatility and reliability of iFEM in SHM applications across various engineering domains, particularly when dealing with complex structural systems, including composite components. Despite these advancements, in the aeronautical and aerospace fields, existing applications have primarily focused on simplified configurations or localized portions of larger assemblies. This represents one of the main limitations highlighted in literature, as such studies often fall short in capturing the full structural and material complexity of real-scale aircraft components—particularly when dealing with composite structures.

In addition to these application-related limitations, another critical aspect to consider in iFEM-based shape sensing is the practical deployment of strain sensors. While in numerical investigations it is often possible to apply strain sensors across the entire structure [2,50,66],

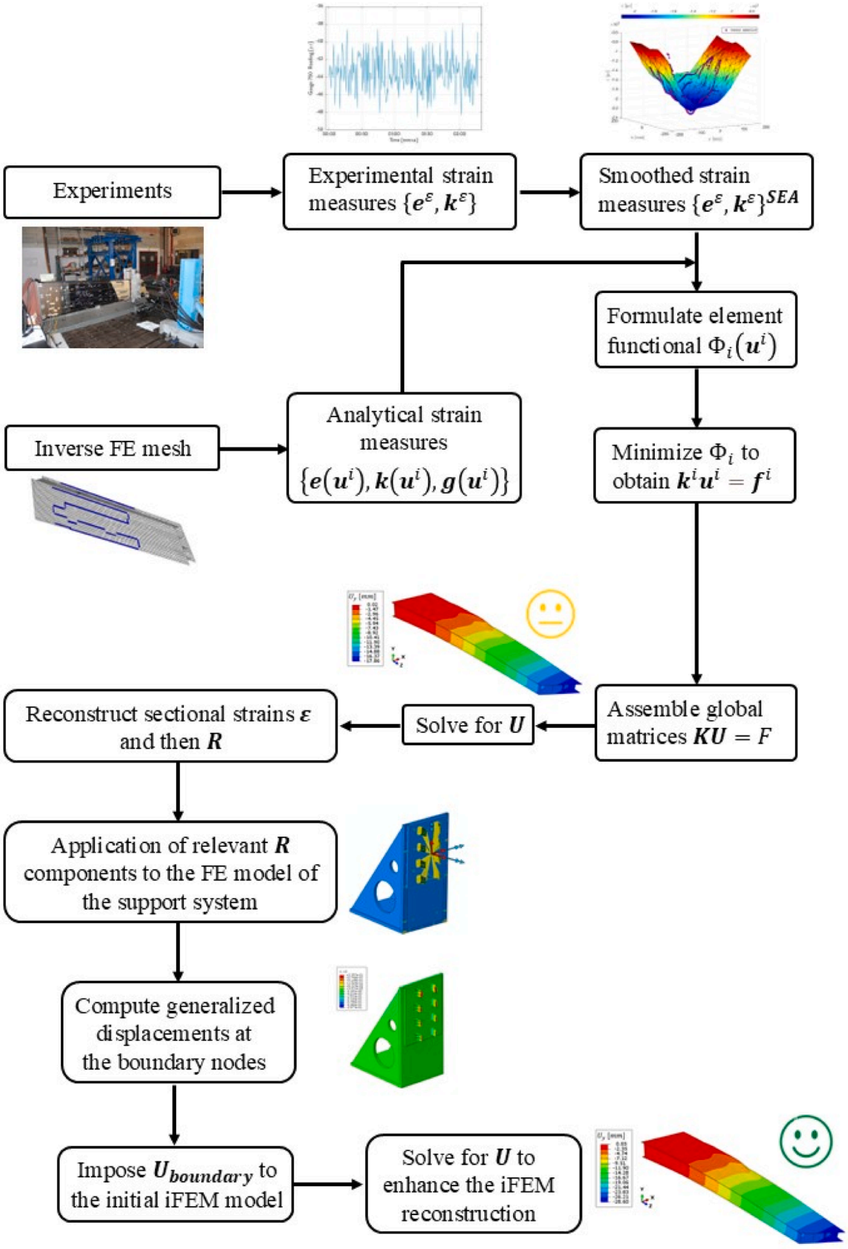

Fig. 1. The proposed research framework, illustrating the main steps from strain data pre-processing to load reconstruction via iFEM.

practical implementations face significant constraints regarding the number and placement of sensors [61,62]. These limitations are typically due to hardware availability and installation challenges, such as restricted access to certain structural areas. As a result, sensors are usually placed over a limited region of the structure, and their positioning must be carefully optimized to capture the strain field as accurately as possible within existing constraints. To improve the quality of the reconstructed displacement field, various pre-extrapolation techniques have proven effective in estimating strain values at locations not directly instrumented with sensors [27,62]. These techniques can be data-driven—based on polynomial fitting or smoothing element analysis (SEA) [27,67–70]—or physics-based, relying on prior knowledge of the system [71,72]. Alternatively, statistical methods such as Gaussian process interpolation have been employed for strain field estimation [73]. In particular, SEA enables the reconstruction of full-field, continuous strain distributions from discrete measurements by minimizing a penalized least-squares functional, ensuring smoothness and stability of the estimated field even with limited sensor data [27]. Despite its potential, only a few studies in literature have applied SEA as a pre-extrapolation method within the iFEM framework, and its use in real-world or full-scale structural applications remains largely unexplored.

Beyond shape sensing, iFEM has also been extended to support damage detection within SHM frameworks, leveraging its ability to capture local variations in structural behavior. Several methodologies have been developed in this context, including the formulation of load-independent damage indices [50,61], the use of damage parameters derived from Von Mises strain to identify local anomalies [74,75], the application of pseudo-excitation-based indices for dynamic assessments [66], and the integration of machine learning techniques, such as artificial neural networks, to enhance detection capabilities [75].

A final aspect, still largely overlooked in the current SHM literature, concerns the uncertainty and potential degradation of boundary conditions over time. This issue, although often neglected, can significantly

Table 1
Summary of the data processing chain adopted in this work, from distributed strain measurements to displacement reconstruction and validation.

Stage	Input data	Processing step	Output/Purpose
Sensor acquisition	Distributed strain from optical fibers	Interrogator by LUNA system	Raw strain profiles
Pre-processing	Raw strain profiles	Noise filtering and referencing	Clean strain signals
SEA	Clean strain signals	Strain pre-extrapolation on SEA mesh	Smoothed strain field
iFEM	Smoothed strain field	Inverse finite element reconstruction	Displacement and internal force fields
Validation	Reconstructed displacement field	Comparison with experimental data	Accuracy assessment

compromise the accuracy of shape sensing and damage detection strategies based on iFEM. In real-world structures—particularly in aerospace applications—boundary connections are rarely as ideal as assumed in numerical models. For instance, the wing-to-fuselage attachments in an aircraft are often idealized as perfectly fixed connections during the design phase. In practice, however, their stiffness is finite and may degrade over time due to bracket flexibility, bolted-joint compliance, fatigue, microcracking, or thermal effects, resulting in partial constraint behavior that significantly influences structural response. If not properly accounted for, such boundary condition uncertainty introduces significant errors in the reconstruction of displacements and strains using iFEM. Similar phenomena are observed in other engineering systems as well, such as steel frames with bolted joints or reinforced concrete beams embedded in aging infrastructure. Nevertheless, most existing studies either neglect this issue or address it indirectly through modal identification or flexibility-based approaches, which often require prior knowledge of external loads or material properties. Only a few attempts, such as the vision-based methodology proposed by Colombo et al. [61] for composite plates, have tried to tackle this challenge within the iFEM framework. Yet, their applicability to full-scale or in-service structures remains limited due to practical constraints like sensor accessibility or camera positioning. Therefore, explicitly addressing the variability and uncertainty of boundary conditions is crucial to enhance the reliability and robustness of iFEM-based SHM in operational scenarios—particularly for complex, full-scale composite structures in aerospace applications.

To address the limitations previously discussed, the present study introduces a novel combined numerical–experimental methodology for shape sensing on a representative full-scale Unmanned Aerial Vehicle (UAV) stabilizer made of composite material. The proposed approach is designed to tackle key challenges identified in literature, including the lack of full-scale experimental validation on complex composite structures, the limited use of pre-extrapolation techniques such as SEA within the iFEM framework and finally the influence of uncertain or degraded boundary conditions on reconstruction accuracy. The key innovations of the proposed approach can be summarized as follows:

1. Experimental validation of the iFEM methodology on a full-scale aircraft composite stabilizer in a cantilever configuration, including real sensor deployment (LUNA distributed fiber optic sensors) under bending and torsional loads induced by two actuators.
2. Application of a modified SEA-based strain pre-extrapolation, integrated within the iFEM framework, applied sequentially on multiple structural planes and accounting for the variable thickness of the demonstrator to enhance reconstruction accuracy under sparse sensor configurations.
3. Development of a numerical methodology with an explicit model of the structural support system, loaded with internal actions reconstructed by the iFEM, to account for non-ideal boundary conditions and enhance reconstruction accuracy in realistic configurations.

The paper is structured as follows. Section 2 presents the theoretical framework of the iFEM formulation, SEA pre-extrapolation strategy and its coupling with non-ideal boundary conditions. Section 3 outlines the numerical and experimental studies, detailing the experimental sensor network, the acquisition of strain measurements, the experimental tests, the support system FE model and their integration into the iFEM framework. Also, it discusses the results obtained, including the reconstruction of full-field displacement and strain for various scenarios investigated, accounting also for the uncertainty in the definition of the boundary conditions. Section 4 concludes the paper, summarizing key findings and their implications for future research and applications.

2. Research framework methodology

The following sections describe the various steps of the proposed framework. Initially, the overall methodology is introduced and illustrated through a schematic representation. Subsequently, the analytical formulation of the inverse iFEM for shell structures is presented, followed by the description of the SEA technique adopted for strain field pre-extrapolation. Finally, the procedure for reconstructing internal loads from the iFEM output is outlined.

2.1. Overall research framework

The overall research framework is schematically illustrated in Fig. 1 and the main steps of the data processing chain are summarized in Table 1.

As illustrated in Fig. 1, the proposed research framework is structured into several phases. The process starts with the acquisition of strain data from a limited number of sensors strategically placed on the surface of the monitored structure (stabilizer) during various experimental tests.

Due to practical constraints—such as sensor cost, accessibility, and installation limitations—the spatial resolution of the experimental strain data is typically insufficient for direct use in iFEM methodology with accurate results. To address this, the SEA technique is applied to the stabilizer structure as a pre-processing step. SEA enables the reconstruction of a smooth and continuous strain field over the entire structural domain, extrapolating information in regions not directly instrumented. Since the structure under investigation is complex and composed of multiple interconnected surfaces, only a subset of these can be instrumented with strain sensors. As a result, the SEA procedure is applied individually to each surface. The process begins with the sensorized surfaces, where actual strain data is available, and then proceeds to the non-sensorized ones. For each unsensed surface, the SEA uses the extrapolated results from the previously processed surfaces as input at the nodes shared between adjacent regions. This enhanced strain field provides the necessary input for the subsequent application of the iFEM, which is then used to reconstruct the complete displacement field of the structure in a model-based and load-independent manner.

The previous reconstruction was carried out under the assumption of ideal boundary conditions (full clamp along the root section of the stabilizer, as a cantilever beam). However, in real applications, the structure under investigation is often connected to other structural components whose mechanical behavior may not ensure ideal constraints. This can be due to connection flexibility, assembly tolerances, or degradation effects. To improve the accuracy of the reconstruction, it is therefore essential to identify which components of the connection may compromise the ideal constraint assumption. This assessment can

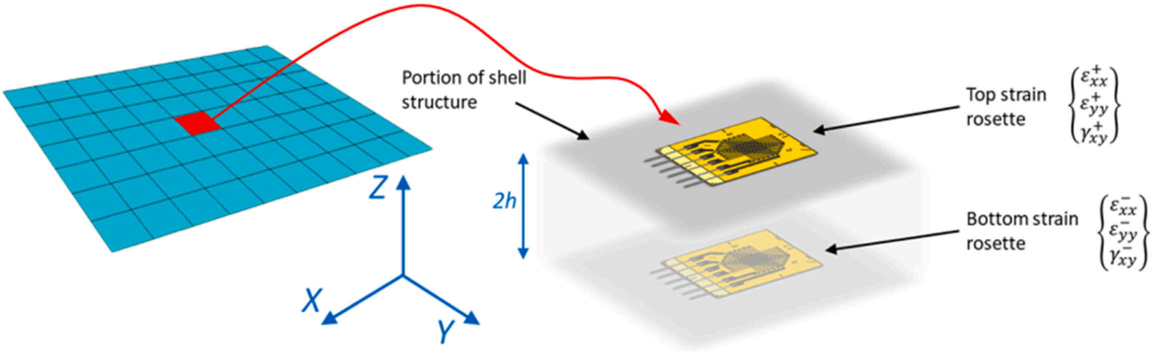

Fig. 2. Discrete sensor location both on the top and on the bottom surface of the shell structure. Adapted from [1].

be supported by strategically placing sensors on the connection itself to detect which parts are more susceptible to deformation or relative motion, thus indicating a deviation from ideal boundary behavior. A way to address this is to develop a static numerical model of the support system—in this case, the support system of the stabilizer—and apply to it the internal actions reconstructed through iFEM. In fact, based on the reconstructed displacement field, the internal force resultants—namely membrane forces, bending moments, and transverse shear forces—are calculated using classical plate theory formulation, in combination with the known material properties of the structure. As said, the last step requires accurate knowledge of the material properties of both the monitored structure and its support system—information that is typically well known during the design phase.

The model of the support system allows for the estimation of the generalized displacements at the stabilizer–support interface, which represent the constraint deformations or boundary flexibility (i.e., the actual compliance of the connection). These generalized displacements $U_{boundary}$ are then imposed as boundary conditions in a refined iFEM model of the stabilizer, enhancing the accuracy of the final displacement reconstruction and making the method suitable for realistic real-world structural configurations.

It is important to note, however, that the initial reconstruction of the displacement field—and consequently of the strain field and internal actions—is inherently limited by the accuracy of the assumed boundary conditions. If the initial boundary conditions are not representative of the actual constraint behavior, the reconstructed fields will carry corresponding inaccuracies. For this reason, the proposed procedure—starting with an initial iFEM reconstruction, followed by the estimation of generalized displacements from the support model, and then applying these as non-ideal boundary conditions in an updated iFEM model—can be iteratively repeated. This iterative loop allows for progressive refinement of the reconstructed fields and increased fidelity of the result.

This refinement loop should be understood as a correction strategy for boundary conditions rather than as a classical iterative solver. First, the stabilizer is reconstructed with ideal BCs, which capture the global kinematics but neglect the compliance of the support. Internal forces from this reconstruction are applied to a support model to extract realistic displacements and rotations, which are then imposed as non-ideal BCs in a refined iFEM run. In the present case, this two-step procedure was sufficient, with validation at the actuator locations confirming the improved accuracy. In cases where the initial reconstruction with ideal BCs is less accurate, additional cycles may be performed until the displacement fields stabilize within measurement uncertainty.

Finally, it is worth highlighting that this framework is suitable for real-time implementation, as both the iFEM algorithm and the static model of the support system are computationally efficient. This enables continuous updates and progressive improvement of the reconstruction quality in real-time monitoring scenarios.

2.2. *iFEM formulation for shell structures*

This section provides a general overview of the iFEM methodology [28,29], whereas readers interested in the specific formulation of the iQS4 element (based on Mindlin theory as its kinematic framework) can refer to the more detailed discussions in [41,43]. Consider a shell structure discretized using inverse elements (Fig. 2); in this study, the iQS4 element is employed [41]. The displacement field is reconstructed from measured strain data by minimizing the least-squares functional presented in Eq. (1). This functional quantifies the discrepancy between the strain field obtained from sensors $(\cdot^{\varepsilon})$ and its numerical counterpart $(\cdot(\boldsymbol{u}))$, which depends on the unknown nodal displacements $\boldsymbol{u}$. Both the measured and computed strain fields are decomposed into three primary components: membrane strain $\boldsymbol{e}$, bending strain $\boldsymbol{k}$, and transverse shear strain $\boldsymbol{g}$. Accordingly, the formulation of the i *th* inverse element is

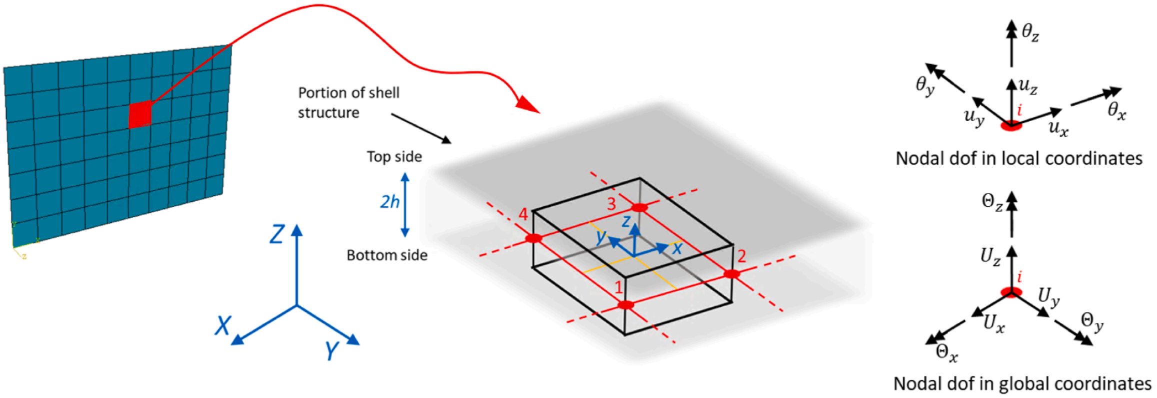

Fig. 3. iQS4 element with global (X,Y,Z) and local (x,y,z) reference systems and the related degrees of freedoms. Numbers 1 to 4 refer to the element nodes. Adapted from [1].

expressed as:

$$\Phi_i(\boldsymbol{u}^i) = \| \boldsymbol{e}(\boldsymbol{u}^i) - \boldsymbol{e}_i^{\varepsilon} \|^2_{\boldsymbol{W}_m^i} + \| \boldsymbol{k}(\boldsymbol{u}^i) - \boldsymbol{k}_i^{\varepsilon} \|^2_{\boldsymbol{W}_b^i} + \| \boldsymbol{g}(\boldsymbol{u}^i) - \boldsymbol{g}_i^{\varepsilon} \|^2_{\boldsymbol{W}_s^i} \tag{1}$$

Where $\| \cdot \|^2_{\boldsymbol{W}}$ is the squared weighted Euclidean norm with the weight matrix $\boldsymbol{W}$. Specifically, $\boldsymbol{W}_m^i$, $\boldsymbol{W}_b^i$, and $\boldsymbol{W}_s^i$ are diagonal matrices of weights for the membrane, bending, and transverse shear strain contributions, respectively. These coefficients control the coherence between the numerical and the experimental strain measurements in the case of sparse sensor networks. In general, a unitary reference value is associated with the elements in which the input strain field component is acquired by physical sensors ($\boldsymbol{e}_i^{\varepsilon}$, $\boldsymbol{k}_i^{\varepsilon}$ and $\boldsymbol{g}_i^{\varepsilon}$), while, in other cases, the coefficients are generally reduced to small values (e.g., 10^{-4}). Notice that each matrix $\boldsymbol{W}$ contains three weights on the main diagonal, which are related to the strain components along the x-axis, the y-axis, and the in-plane shear with respect to the element's local reference system (Fig. 3). Then, if an element is interested by a monoaxial strain sensor, only the weight related to its direction is assigned equal to one and the others are reduced to a small value.

Following an appropriate assembly procedure, the unknown displacement field of the structure is obtained by minimizing the error functional defined in Eq. (1). The formulation of this functional will be discussed in Section 2.2.3, after introducing the input strain field in Section 2.2.1 and its numerical counterpart in Section 2.2.2.

2.2.1. *Input strain formulation*

In the most general case, the input strain field is derived directly from strain measurements acquired on the structure. Sensors are typically installed on the external surfaces of the component, where access for installation and maintenance is more practical, although applications involving embedded sensors have also been reported in the literature [27].

As an example, consider a pair of strain gauge rosettes placed on the outer surfaces of the shell, as illustrated in Fig. 2. The membrane and bending strain components corresponding to the location of the *j-th* sensor within the *i th* inverse element can be expressed as:

$$\boldsymbol{e}_{ij}^{\varepsilon} = \frac{1}{2} \begin{Bmatrix} \varepsilon_{xx}^{+} + \varepsilon_{xx}^{-} \\ \varepsilon_{yy}^{+} + \varepsilon_{yy}^{-} \\ \gamma_{xy}^{+} + \gamma_{xy}^{-} \end{Bmatrix}_j \quad \boldsymbol{k}_{ij}^{\varepsilon} = \frac{1}{2h} \begin{Bmatrix} \varepsilon_{xx}^{+} - \varepsilon_{xx}^{-} \\ \varepsilon_{yy}^{+} - \varepsilon_{yy}^{-} \\ \gamma_{xy}^{+} - \gamma_{xy}^{-} \end{Bmatrix}_j \tag{2}$$

Where $2h$ is the shell thickness at the sensors' location. The computed strain components contain the information of a plane strain tensor and, in case monoaxial strain sensors are used, only one component will be defined, and the others are posed equal to zero.

Furthermore, in practical applications, only a limited number of sensors can be used due to cost, space constraints, and hardware limitations, which restricts the definition of the input strain field. However, for accurate iFEM computations, the input strain field should ideally be defined over all the structure's inverse elements and should adequately capture the strain gradient. Therefore, the sensor network must be carefully designed, and the mesh discretization can be adapted by tuning the element size according to the expected strain variations.

Nevertheless, some elements may remain without input data. To minimize their impact on the global formulation, small weighting coefficients $\boldsymbol{W}_i$ ($i = m, k, s$) can be assigned to those elements. To further enhance the accuracy of iFEM results, the input strain field can be pre-extrapolated in regions where physical sensors are not present, enabling a complete strain field definition over the entire structure. This pre-extrapolation can be performed using different approaches depending on the specific case, as described in the Introduction section. In the case under investigation, strain pre-extrapolation is carried out using the SEA method, the theoretical foundations of which are summarized in Section 2.3.

2.2.2. *Numerical strain formulation*

The numerical strain field required in Eq. (1) is formulated using the element's shape functions, following the standard finite element procedure. A local coordinate system (x, y, z) is defined for each inverse element, with its origin located at the element centroid. In this system, the z-axis represents the out-of-plane direction, spanning the thickness of the shell such that $z \in [-h; \; +h]$, as illustrated in Fig. 3. The local coordinates are obtained from the global reference frame $(X, \; Y, \; Z)$—in which the overall structure is defined—via a transformation matrix that is specific to each element.

Each iQS4 inverse element is composed of four nodes, each one with six degrees of freedom. In particular, each element has 24 degrees of freedom with 3 translations $\boldsymbol{u}_q = \{u_x, \; u_y, \; u_z\}^q$ and 3 rotations $\boldsymbol{\theta}_q = \{\theta_x, \; \theta_y, \theta_z\}^q$ for each element's node $q = (1,2,3,4)$, which are collected into the element's nodal displacement vector $\boldsymbol{u}^i$. Then, the local displacement field within each inverse element is defined through the shape functions $\boldsymbol{N}_q$, $\boldsymbol{L}_q$, and $\boldsymbol{M}_q$ [41] as:

$$u(x, y) = \sum_{q=1}^{4} N_q u_{xq} + \sum_{q=1}^{4} L_q \theta_{zq} \tag{3}$$

$$v(x, y) = \sum_{q=1}^{4} N_q u_{yq} + \sum_{q=1}^{4} M_q \theta_{zq}$$

$$w(x, y) = \sum_{q=1}^{4} N_q u_{zq} - \sum_{q=1}^{4} L_q \theta_{xq} - \sum_{q=1}^{4} M_q \theta_{yq}$$

$$\theta_x(x, y) = \sum_{q=1}^{4} N_q \theta_{xq}$$

$$\theta_y(x, y) = \sum_{q=1}^{4} N_q \theta_{yq}$$

Then, under the hypothesis of plane stress condition and after computing the partial derivatives of the shape functions, the strain field components within each element can be defined as:

$$\boldsymbol{e}(\boldsymbol{u}^i) = \boldsymbol{B}^m \boldsymbol{u}^i$$

$$\boldsymbol{k}(\boldsymbol{u}^i) = \boldsymbol{B}^b \boldsymbol{u}^i$$

$$\boldsymbol{g}(\boldsymbol{u}^i) = \boldsymbol{B}^s \boldsymbol{u}^i \tag{4}$$

Where $\boldsymbol{B}^m$, $\boldsymbol{B}^b$, and $\boldsymbol{B}^s$ are matrices containing the derivatives of the shape functions.

Finally, the numerical strain field can be computed with the following relations in correspondence of the required z coordinate:

$$\begin{Bmatrix} \varepsilon_{xx} \\ \varepsilon_{yy} \\ \gamma_{xy} \end{Bmatrix} = \boldsymbol{e}(\boldsymbol{u}^i) + z \cdot \boldsymbol{k}(\boldsymbol{u}^i)$$

$$\begin{Bmatrix} \gamma_{xz} \\ \gamma_{yz} \end{Bmatrix} = \boldsymbol{g}(\boldsymbol{u}^i) \tag{5}$$

2.2.3. *Matrix formulation*

As previously mentioned, iFEM is based on the minimization of the global functional defined in Eq. (1). However, the formulation discussed thus far has been limited to a single inverse element. Before extending the formulation to account for the contribution of all inverse elements in the mesh, Eq. (1) is reformulated to enable efficient numerical computation. Specifically, the three squared weighted norms are rewritten in terms of normalized Euclidean norms, expressed as:

$$\| \boldsymbol{e}(\boldsymbol{u}^i) - \boldsymbol{e}_i^\varepsilon \|_{\boldsymbol{W}_m^i}^2 = \frac{1}{n} \iint_{A_i} \sum_{j=1}^{n} \left(\boldsymbol{e}(\boldsymbol{u}^i)_j - \boldsymbol{e}_{ij}^\varepsilon \right)^T \boldsymbol{W}_m^i \left(\boldsymbol{e}(\boldsymbol{u}^i)_j - \boldsymbol{e}_{ij}^\varepsilon \right) dxdy \tag{6}$$

$$\| \boldsymbol{k}(\boldsymbol{u}^i) - \boldsymbol{k}_i^\varepsilon \|_{\boldsymbol{W}_b^i}^2 = \frac{(2h)^2}{n} \iint_{A_i} \sum_{j=1}^{n} \left(\boldsymbol{k}(\boldsymbol{u}^i)_j - \boldsymbol{k}_{ij}^\varepsilon \right)^T \boldsymbol{W}_b^i \left(\boldsymbol{k}(\boldsymbol{u}^i)_j - \boldsymbol{k}_{ij}^\varepsilon \right) dxdy$$

$$\| \boldsymbol{g}(\boldsymbol{u}^i) - \boldsymbol{g}_i^\varepsilon \|_{\boldsymbol{W}_s^i}^2 = \frac{1}{n} \iint_{A_i} \sum_{j=1}^{n} \left(\boldsymbol{g}(\boldsymbol{u}^i)_j - \boldsymbol{g}_{ij}^\varepsilon \right)^T \boldsymbol{W}_s^i \left(\boldsymbol{g}(\boldsymbol{u}^i)_j - \boldsymbol{g}_{ij}^\varepsilon \right) dxdy$$

Where A_i is the area of the considered element and n the total number of input strain sensors within the same. Then, after substituting the input and the numerical strain components previously developed in Sections 2.2.1 and 2.2.2, respectively, the least-square functional can be expressed as:

$$\Phi_i(\boldsymbol{u}^i) = \boldsymbol{u}^{i^T} \boldsymbol{k}^i \boldsymbol{u}^i - 2\boldsymbol{u}^{i^T} \boldsymbol{f}^i + \xi^i \tag{7}$$

In which:

$$\boldsymbol{k}^i = \iint_{A_i} \left(\boldsymbol{B}^{\boldsymbol{m}^T} \boldsymbol{W}_m \boldsymbol{B}^{\boldsymbol{m}} + (2h)^2 \boldsymbol{B}^{\boldsymbol{b}^T} \boldsymbol{W}_b \boldsymbol{B}^{\boldsymbol{b}} + \boldsymbol{B}^{\boldsymbol{s}^T} \boldsymbol{W}_s \boldsymbol{B}^{\boldsymbol{s}} \right) dxdy \tag{8}$$

$$\boldsymbol{f}^i = \frac{1}{n} \iint_{A_i} \sum_{j=1}^{n} \left(\boldsymbol{B}^{\boldsymbol{m}^T} \boldsymbol{W}_m \boldsymbol{e}_{ij}^\varepsilon + (2h)^2 \boldsymbol{B}^{\boldsymbol{b}^T} \boldsymbol{W}_b \boldsymbol{k}_{ij}^\varepsilon + \boldsymbol{B}^{\boldsymbol{s}^T} \boldsymbol{W}_s \boldsymbol{g}_{ij}^\varepsilon \right) dxdy$$

$$\xi^i = \frac{1}{n} \iint_{A_i} \sum_{j=1}^{n} \left(\boldsymbol{e}_{ij}^{\varepsilon^T} \boldsymbol{W}_m \boldsymbol{e}_{ij}^\varepsilon + (2h)^2 \boldsymbol{k}_{ij}^{\varepsilon^T} \boldsymbol{W}_b \boldsymbol{k}_{ij}^\varepsilon + \boldsymbol{g}_{ij}^{\varepsilon^T} \boldsymbol{W}_s \boldsymbol{g}_{ij}^\varepsilon \right) dxdy$$

The integrals involved can be efficiently evaluated using numerical techniques such as Gauss quadrature—for instance, by employing four integration points per inverse element to ensure sufficient accuracy. A standard assembly procedure is then used to incorporate the contributions of all inverse elements in the structure, resulting in the global form of Eq. (7). This global functional is subsequently minimized with respect to the global displacement field, i.e., by imposing $\partial\Phi / \partial \boldsymbol{U} = 0$, leading to the following system of equations:

$$\boldsymbol{K}\boldsymbol{U} = \boldsymbol{F} \tag{9}$$

where $\boldsymbol{K}$ is a matrix linking the nodal displacement $\boldsymbol{U}$, in global coordinates (U_x, U_y, U_z, Θ_x, Θ_y, and Θ_z for each node), with the vector $\boldsymbol{F}$, which is a function of the input strain field. Notice that the matrix $\boldsymbol{K}$ depends on the structure's element discretization and on the sensor network configuration, while $\boldsymbol{F}$ only depends on the input strain measurements. However, the matrix $\boldsymbol{K}$ is singular and it will lead to a rigid motion of the structure if unconstrained; thus, after the definition of problem-specific boundary conditions, the unconstrained (free) nodal displacements can be computed as:

$$\boldsymbol{K}_{\boldsymbol{FF}} \boldsymbol{U}_{\boldsymbol{F}} = \boldsymbol{F}_{\boldsymbol{F}} \Rightarrow \boldsymbol{U}_{\boldsymbol{F}} = \boldsymbol{K}_{\boldsymbol{FF}}^{-1} \boldsymbol{F}_{\boldsymbol{F}} \tag{10}$$

Finally, after the computation of the structure's displacement field, the numerical strain can be computed on the whole structure through Eq. (5).

2.3. Review of smoothing element analysis (SEA) formulation for strain pre-extrapolation

To enhance the robustness of shape-sensing procedures when only a limited number of strain sensors are available, the present study adopts the SEA as a pre-processing step for experimental strain data. SEA is a finite element-based technique that minimizes a penalized least-squares functional to generate smooth approximations of discrete input data. In this context, the experimental strain components—typically collected from strain gauges or fiber Bragg grating (FBG) sensors—are transformed into continuous functions of the spatial coordinates over the entire domain of the structure.

As an example, consider a configuration in which strain gauges or rosettes or fiber Bragg grating (FBG) are mounted on the top and bottom surfaces of the plate or composite laminate, while no sensors are embedded, for simplicity, within the laminate, as illustrated in Fig. 2. The discrete experimental strain data can be represented as a vector $\boldsymbol{\varepsilon}_i^\chi \equiv \left[(\varepsilon_{xx}^\chi)_i \quad (\varepsilon_{yy}^\chi)_i \quad (\gamma_{xy}^\chi)_i \right]^T$, where the subscript $i = 1, 2, \ldots, n$ identifies the in-plane measurement location, and the subscript $\chi = +, -$ refers, as always, to the measurement position on the top surface and bottom surface, respectively.

Here, $(\varepsilon_{xx}^\chi)_i$ and $(\varepsilon_{yy}^\chi)_i$ denote the normal strains along the x and y directions, while $(\gamma_{xy}^\chi)_i$ corresponds to the engineering shear strain in the xy-plane (see Fig. 3). Prior to performing the iFEM analysis, these discrete experimental data can be analytically processed through the SEA, which enables the reconstruction of a full-field strain distribution over the plate domain and reduces the approximation error associated with discrete sensor measurements.

Through SEA, the strain components acquired from strain gauges and FBG sensors are converted into continuous functions of the spatial coordinates across the reference plane of the plate, expressed as $\boldsymbol{\varepsilon}^\chi \equiv \left[\varepsilon_{xx}^\chi(\boldsymbol{x}) \quad \varepsilon_{yy}^\chi(\boldsymbol{x}) \quad \gamma_{xy}^\chi(\boldsymbol{x}) \right]^T$ ($\chi = +\,,\,-$). This process yields C^1-continuous strain fields, meaning that their first spatial derivatives are C^0-continuous. For detailed formulations and mathematical foundations of the SEA method, including three- and four-node smoothing elements, the reader is referred to [67–50].

For a concise notation, let ε_i^h denote a generic term from the discrete set of experimental strain data, for example $\varepsilon_i^h \equiv \left(\gamma_{xy}^-\right)_i$, $\varepsilon_i^h \equiv \left(\varepsilon_{xx}^j\right)_i$ ($i = 1, 2, 3, \ldots, n$), etc. The continuous strain field resulting from the application of SEA can then be written as $\varepsilon_i^h \rightarrow \varepsilon(\boldsymbol{x}) \equiv \varepsilon$. For a single smoothing element, the corresponding penalized discrete least-squares error functional can be expressed following [67] as:

$$F_{SEA} = \frac{1}{n_{e,SEA}} \sum_{i=1}^{n_{e,SEA}} \left[\varepsilon(\boldsymbol{x}_i) - \varepsilon_i^h \right]^2 + \alpha \int_{A_{e,SEA}} \left[\left(\varepsilon_{,x} - \kappa_x \right)^2 + \left(\varepsilon_{,y} - \kappa_y \right)^2 \right] dA_{e,SEA}$$
$$+ \; \beta A_{e,SEA} \int_{A_{e,SEA}} \left[\left(\kappa_{x,x} \right)^2 + \left(\kappa_{y,y} \right)^2 + \frac{1}{2} \left(\kappa_{x,y} + \kappa_{y,x} \right)^2 \right] dA_{e,SEA} \tag{11}$$

In this context, the symbol $\varepsilon(\boldsymbol{x}_i)$ denotes the analytical counterpart of the discrete strain data ε_i^h at the point $\boldsymbol{x}_i$, while the operator $(\cdot)_{,\alpha} \equiv \frac{\partial(\cdot)}{\partial x_\alpha}$ indicates partial differentiation with respect to the in-plane coordinates. The term $A_{e,SEA}$ represents the area of the smoothing element. In Eq. (11), $\kappa_x \equiv \kappa_x(\boldsymbol{x})$ and $\kappa_y \equiv \kappa_y(\boldsymbol{x})$ are the analytical counterparts of the first-order derivatives of the discrete strain data ε_i^h with respect to x and , respectively. The first term of Eq. (11) corresponds to a discrete least-squares functional that enforces consistency between the smoothed strain field and the experimental measurements. The second term introduces a penalty that promotes smoothness by approximating the strain field's derivatives (κ_x, κ_y) with respect to the in-plane coordinates. The third term imposes a curvature-control constraint that mitigates local errors in the spatial distribution of the experimental strain data.

The influence of these regularization terms is governed by the dimensionless parameters α and β, which regulate the smoothness and curvature constraints, respectively. Achieving C^1-continuity of the strain field $\varepsilon(\boldsymbol{x})$ and C^0-continuity of its derivatives $\kappa_i(\boldsymbol{x})$ across the SEA domain can be accomplished by choosing appropriate values of α and β. Typically, α is selected from values such as 10^2, 10^3, and so on, while β is chosen from smaller values like 10^{-3}, 10^{-4}, etc.

When experimental strain data is uniformly distributed across each smoothing element (i.e., with similar numbers and locations of sensors), the influence of the penalty parameter α on the least-squares term is

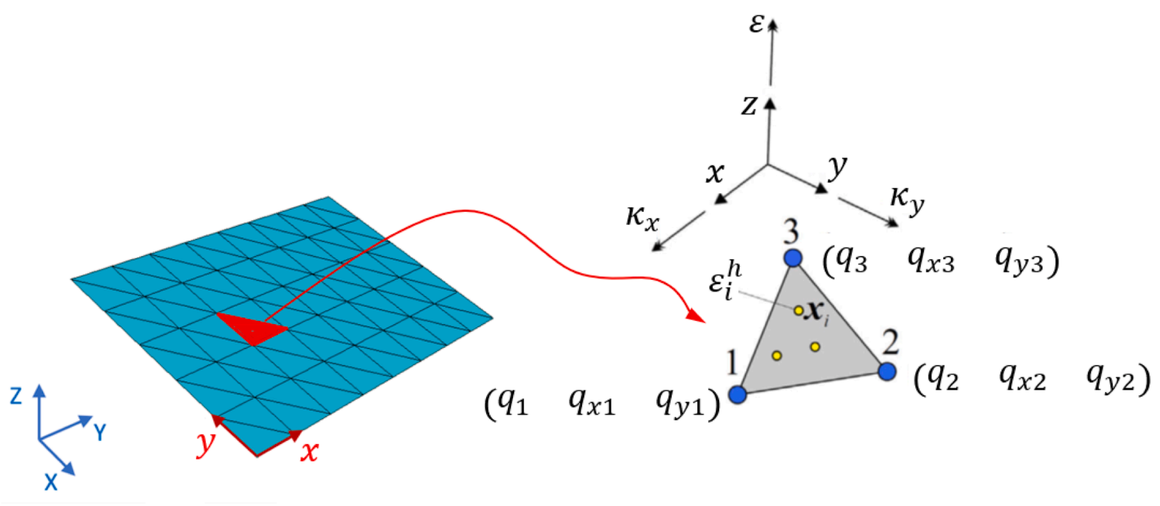

Fig. 4. A generic three-node triangular smoothing element with associated nodal degrees of freedom of a simple plate structure. Adapted from [27].

negligible for values greater than 0.1. As such, the value of $\alpha = 1$ is generally sufficient in well-sampled configurations. On the other hand, when few sensor data points are available—such as one or two per smoothing element—setting a small value for the curvature-control parameter β helps stabilize the SEA formulation. Further guidance on selecting suitable values for these parameters is provided in references [67–68].

The smoothed strain field $\varepsilon(\boldsymbol{x})$ and its corresponding analytical derivatives $\kappa_i(\boldsymbol{x})$ can be approximated using element-wise interpolation. To this end, the three-node triangular smoothing element introduced in [69] is employed, and the smoothed quantities are defined as:

$$\varepsilon(\boldsymbol{x}) = \sum_{i=1}^{3}\left(\zeta_i(\boldsymbol{x})q_i + \zeta_{xi}(\boldsymbol{x})q_{xi} + \zeta_{yi}(\boldsymbol{x})q_{yi}\right) = \boldsymbol{N}\boldsymbol{q}^e$$

$$\kappa_i(\boldsymbol{x}) = \sum_{i=1}^{3}\zeta_i(\boldsymbol{x})q_{ji} \ (j=1,2) \tag{12}$$

With $\boldsymbol{N} = \begin{bmatrix}\boldsymbol{N}_1 & \boldsymbol{N}_2 & \boldsymbol{N}_3\end{bmatrix}^T$, $\boldsymbol{N}_i = \begin{bmatrix}\zeta_i & \zeta_{xi} & \zeta_{yi}\end{bmatrix}$, $\boldsymbol{q}^e = \begin{bmatrix}\boldsymbol{q}_1 & \boldsymbol{q}_2 & \boldsymbol{q}_3\end{bmatrix}^T$ and $\boldsymbol{q}_i = \begin{bmatrix}q_i & q_{xi} & q_{yi}\end{bmatrix}$ considering $(i = 1,2,3)$. The vector $\boldsymbol{q}_i$ contains the nodal degrees of freedom as depicted in Fig. 4. These nodal degrees of freedom $\left(q_i \quad q_{xi} \quad q_{yi}\,; i = 1,2,3\right)$ correspond to the smoothed strain component and its derivatives with respect to the x and y coordinates, respectively. Also, $\boldsymbol{N}_i$ vector contains the shape functions of the element that are the linear and quadratic functions of the local coordinates of the element. For brevity, the explicit expressions for the calculation of the functions inside $\boldsymbol{N}_i$ are omitted here and can be found in standard references, such as [27].

Substituting Eq. (12) into Eq. (11) and minimizing the resultant equation with respect to the unknown nodal degrees of freedom of the triangular smoothing element, $\boldsymbol{q}^e$, a set of final equations can be obtained in the following compact form:

$$\frac{\partial F_{SEA}(\boldsymbol{q}^e)}{\partial \boldsymbol{q}^e} = 0 \Rightarrow \boldsymbol{A}^e\boldsymbol{q}^e = \boldsymbol{H}^e \Rightarrow \boldsymbol{q}^e = \left(\boldsymbol{A}^e\right)^{-1}\boldsymbol{H}^e \tag{13}$$

Where the right-hand-side vector $\boldsymbol{H}^e$ depends on the discrete experimental strain data, defined as:

$$\boldsymbol{H}^e = \frac{1}{n_{e,SEA}}\sum_{i=1}^{n_{e,SEA}}\boldsymbol{N}(\boldsymbol{x}_i)^T\varepsilon_i^h \tag{14}$$

Whereas the left-hand-side matrix $\boldsymbol{A}^e$ includes the squared values of the shape functions evaluated at the strain sensor positions $\boldsymbol{x}_i$, as well as the squared terms of their first-order derivatives, expressed as:

$$\boldsymbol{A}^e = \frac{1}{n_{e,SEA}}\sum_{i=1}^{n_{e,SEA}}\boldsymbol{N}(\boldsymbol{x}_i)^T\boldsymbol{N}(\boldsymbol{x}_i) + \alpha\int_{A_{e,SEA}}\boldsymbol{B}_\alpha^T\boldsymbol{B}_\alpha dA_{e,SEA}$$

$$+\beta A_{e,SEA}\int_{A_{e,SEA}}\boldsymbol{B}_\beta^T\boldsymbol{D}_\beta\boldsymbol{B}_\beta dA_{e,SEA} \tag{15}$$

Where the matrices $\boldsymbol{B}_\alpha$, $\boldsymbol{B}_\beta$ and $\boldsymbol{D}_\beta$ are computed using the standard formulations reported in [27], which are not explicitly recalled here for brevity, as they are well-established in the SEA strategy.

The matrix $\boldsymbol{A}^e$ is square, symmetric, and exhibits a banded structure. When the smoothing domain of the plate is discretized into multiple smoothing elements, a global system of equations is assembled by combining the contributions of each element. This global system can then be efficiently solved to determine the unknown nodal degrees of freedom associated with smoothing discretization.

Different from the iFEM, in the SEA the problem is solved for all degrees of freedom. Indeed, the application of boundary conditions is not necessary for the SEA. However, if the exact behavior of the field is

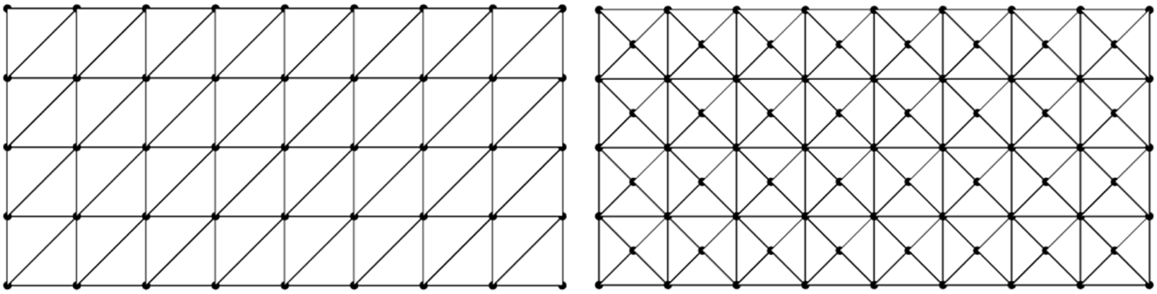

(a) (b)

Fig. 5. SEA mesh configurations: (a) structured triangular and (b) cross-pattern.

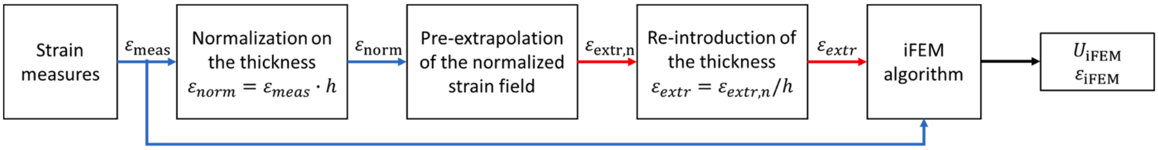

Fig. 6. Scheme of the iFEM steps with the pre-extrapolation procedure for variable thickness structures studied in [76].

known in some regions, some constraints can be applied as in any finite element analysis.

A final aspect to be discussed for SEA implementation is the definition of the mesh. The following two main approaches can be carried out: a structured triangular configuration, in which all common edges between adjacent triangles are parallel, and a cross-pattern configuration, as illustrated in Fig. 5.

Generally, the cross-pattern configuration is considered a better option due to its higher symmetry, which enhances the mesh's ability to deform according to its degrees of freedom. A mixed configuration is also feasible, with some regions of the structure meshed using structured triangular elements and others adopting the cross-pattern layout. Regardless of the chosen mesh configuration, a key parameter is the mesh size [62]. The SEA mesh should be sized appropriately, in coherence with the spatial distribution of the available measurements. A higher number of elements increases the ability to capture steep strain gradients. However, an excessively refined mesh may result in many elements lacking measurement coverage, which can reduce the accuracy of the field reconstruction. Therefore, the mesh size should be optimized by balancing the expected strain field gradients and the density of the sensor network. Ideally, each element should be covered by at least one measurement. Generally, the SEA mesh is typically coarser than the corresponding iFEM mesh.

Closely related to the pre-extrapolation step is the following important consideration: in general, given a certain level of internal action in a shell component (e.g., axial force or bending moment), the resulting deformation is inversely proportional to material thickness. In other words, regions with greater thickness tend to exhibit lower strain under the same loading conditions. Therefore, when pre-extrapolating the strain field from sensor data distributed across regions with varying thicknesses, the algorithm should account for the fact that strain magnitudes are inherently linked to the local thickness of the shell. However, as can be seen from the SEA equations introduced earlier, the structural thickness does not explicitly appear in the formulation. This omission may lead to inconsistencies when extrapolating strain fields across heterogeneous regions, and it highlights the need for incorporating thickness effects into the SEA framework for more accurate strain reconstruction.

To overcome this limitation, the formulation proposed by Poloni et al. [76] has been adopted. This approach introduces a thickness-weighted correction into the SEA framework, allowing the pre-extrapolated strain field to be properly scaled according to the local thickness of the shell regions involved. This improvement is particularly relevant for the stabilizer case study, where the skins do not have uniform thickness, as described in detail in Section 3. When applying pre-extrapolation to this structure (and to its upper and lower skins), it is essential to account for their variable geometry. Although the external loading of the stabilizer induces a global bending deformation, the skins—being significantly thinner than the distance separating them—can be considered to respond primarily through in-plane (membrane) strains rather than bending. As a result, in this work, only the effect of thickness on membrane strain is considered in the extrapolation. Furthermore, since sensors are placed only on the external surfaces of the skin due to accessibility constraints, the strain values on the internal surfaces must be inferred. Assuming membrane-dominated behavior, internal and external values are considered equal (i.e., $\varepsilon^- = \varepsilon^+$), which is a reasonable simplification for the purpose of this study.

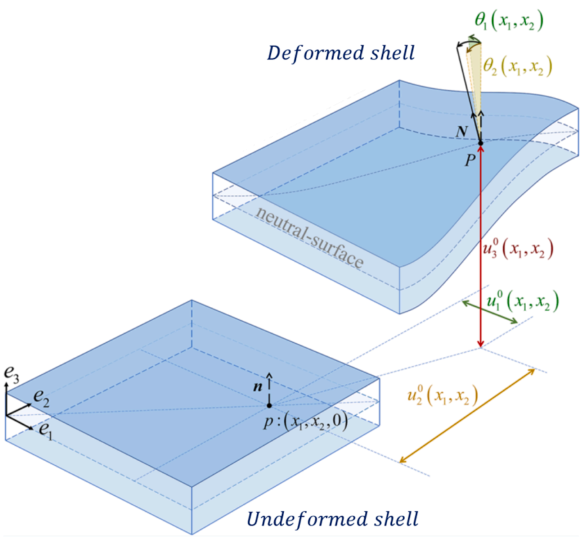

Fig. 7. The kinematics of a shell structure. Adapted from [77].

The detailed procedure proposed in [76] is not recalled here; the reader is referred to the original reference for a complete description of the methodology and its implementation Fig. 6

While local bending effects may arise in specific loading scenarios, they are inherently embedded in the measured strain field and are thus accounted for in the iFEM reconstruction. For extreme cases involving impact or concentrated out-of-plane forces, bending contributions may become more relevant. The present SEA–iFEM workflow can be extended with higher-order enrichment strategies to address such conditions, and we are currently preparing a follow-up study specifically targeting impact loading, where the role of local bending will be more explicitly analyzed.

2.4. *Internal forces reconstruction*

The reconstruction of displacement and strain fields using the iFEM algorithm provides valuable information for SHM in engineering applications, but it is not the only data that can be retrieved. This section presents the strategy adopted in this study to reconstruct the internal forces within transverse structural sections, based on the strain field obtained through iFEM. This approach takes advantage of the known material properties and the reconstructed strain distribution provided by the iFEM algorithm. To compute the sectional internal forces, the authors rely on classical plate and shell theories—namely, the Kirchhoff–Love or Reissner–Mindlin formulations—as illustrated in Fig. 7 [2, 77]. Depending on the structural characteristics of the problem, one theory may be more suitable than the other. In the present case, due to the slender and thin-walled nature of the stabilizer, the Kirchhoff–Love theory is adopted as the reference formulation. For completeness, the full mathematical formulation is reported in the following section.

For this case, the classical vector of sectional strains $\boldsymbol{\varepsilon} = [\varepsilon_1, \varepsilon_2, \gamma_{12}, \kappa_1, \kappa_2, \kappa_{12}, \gamma_1, \gamma_2]^T$ can be defined, where $\varepsilon_1, \varepsilon_2, \gamma_{12}$ are the membrane strains, κ_1, κ_2 are the bending curvatures, κ_{12} is the twisting curvature and finally γ_1, γ_2 are the transverse shear strains (the latter

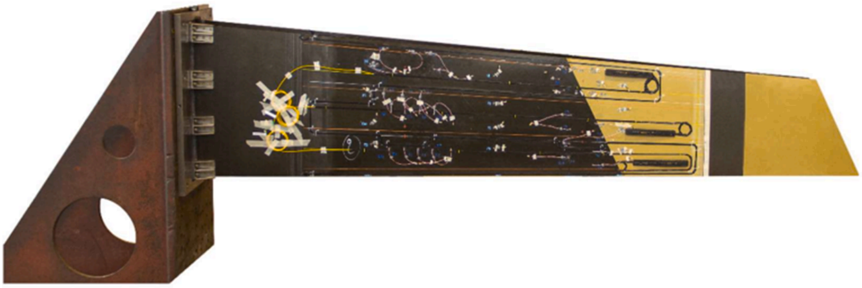

Fig. 8. Test sample and its supporting system (view from the upper skin side).

negligible when the Kirchhoff–Love model is applied).

Accordingly, the vector of the generalized stresses $\boldsymbol{R} = [N_1, N_2, N_{12}, M_1, M_2, M_{12}, Q_1, Q_2]^T$ can be defined as:

$$(N_1, N_2, N_{12}, Q_1, Q_2) = \int (\sigma_1, \sigma_2, \tau_{12}, \tau_{13}, \tau_{23}) dx_3 \tag{16}$$

$$(M_1, M_2, M_{12}) = \int (\sigma_1, \sigma_2, \tau_{12}) x_3 dx_3 \tag{17}$$

Sectional stiffnesses/flexibilities are defined to relate sectional generalized stresses to sectional strains. For a uniform thick shell with an isotropic material (for instance steel or aluminum), such a relation can be expressed as:

$$\begin{bmatrix} \varepsilon_1 \\ \varepsilon_2 \\ \gamma_{12} \\ \kappa_1 \\ \kappa_2 \\ \kappa_{12} \\ \gamma_1 \\ \gamma_2 \end{bmatrix} = \begin{bmatrix} \dfrac{1}{Eh}\begin{bmatrix} 1 & -\nu & 0 \\ -\nu & 1 & 0 \\ 0 & 0 & 2(1+\nu) \end{bmatrix} & 0 & 0 \\ 0 & \dfrac{12}{Eh^3}\begin{bmatrix} 1 & -\nu & 0 \\ -\nu & 1 & 0 \\ 0 & 0 & 2(1+\nu) \end{bmatrix} & 0 \\ 0 & 0 & \dfrac{1}{kGh}\begin{bmatrix} 1 & 0 \\ 0 & 1 \end{bmatrix} \end{bmatrix} \begin{bmatrix} N_1 \\ N_2 \\ N_{12} \\ M_1 \\ M_2 \\ M_{12} \\ Q_1 \\ Q_2 \end{bmatrix} \tag{18}$$

Where k is the well-known shear factor, E the Young's modulus, G the shear modulus and finally h the thickness of the plate.

Since the structure under investigation is composed of composite laminated materials (as described in detail in Section 3), Eq. (18) must be generalized to account for the anisotropic and layerwise-varying properties of each ply. In this context, the relation between generalized stresses and strains is governed by the laminate stiffness matrices $\boldsymbol{A}$, $\boldsymbol{B}$, $\boldsymbol{D}$, and $\boldsymbol{S}$, which relate membrane forces, bending moments, transverse shear forces, and membrane-bending coupling effects to the corresponding strain components. Specifically, $\boldsymbol{A}$, $\boldsymbol{B}$, and $\boldsymbol{D}$ describe the in-plane, coupling, and bending stiffnesses of the laminate, respectively, while $\boldsymbol{S}$ represents the transverse shear stiffness matrix and accounts for shear deformation through the thickness of the shell or plate. The updated version of Eq. (18) for composites is the following:

$$\begin{bmatrix} \varepsilon_1 \\ \varepsilon_2 \\ \gamma_{12} \\ \kappa_1 \\ \kappa_2 \\ \kappa_{12} \\ \gamma_1 \\ \gamma_2 \end{bmatrix} = \begin{bmatrix} \boldsymbol{A} & \boldsymbol{B} & 0 \\ \boldsymbol{B} & \boldsymbol{D} & 0 \\ 0 & 0 & \boldsymbol{S} \end{bmatrix}^{-1} \begin{bmatrix} N_1 \\ N_2 \\ N_{12} \\ M_1 \\ M_2 \\ M_{12} \\ Q_1 \\ Q_2 \end{bmatrix} \tag{19}$$

The matrices $\boldsymbol{A}$, $\boldsymbol{B}$, $\boldsymbol{D}$, and $\boldsymbol{S}$ are computed by integrating the transformed reduced stiffness of each ply through the laminate thickness, considering the ply orientations, material properties, and stacking sequence. This generalized formulation enables the accurate reconstruction of internal forces in laminated composite structures, starting from the strain field obtained through the iFEM algorithm, provided that the material properties and stacking sequence of the laminate are fully known.

Within the framework, a linear elastic behavior of the structure is assumed. For a given section of interest, the corresponding internal forces are calculated as the sum of contributions from each element intersected by the section. Starting from the strain field $\boldsymbol{\varepsilon}_{iFEM}$ reconstructed by the iFEM, the contributions $\boldsymbol{R} = [N_1, N_2, N_{12}, M_1, M_2, M_{12}, Q_1, Q_2]^T$ of individual elements are determined by applying Eq. (20). Finally, the internal forces of the section considered are obtained as the sum of the products of the generalized stresses and the respective lengths of each element.

It is important to remark that, while the displacement field reconstructed by iFEM is independent of material properties, the subsequent step of internal force reconstruction relies on the laminate stiffness matrices $[\boldsymbol{A}, \boldsymbol{B}, \boldsymbol{D}, \boldsymbol{S}]$. Consequently, uncertainties in ply properties or in the stacking sequence definition may affect the accuracy of the reconstructed internal forces. In the present study, the manufacturer's material data and lay-up were considered as reference, whereas a detailed sensitivity analysis to such uncertainties is left for future investigations.

3. Case study

This section introduces the case study and provides a comprehensive overview of the experimental and numerical activities carried out. The specimen and the corresponding experimental setup are described in Section 3.1, followed by the experimental quasi-static tests in Section 3.2. Section 3.3 presents the sensor network and its installation on the structure, while Section 3.4 describes the sources of uncertainty in the boundary conditions. Finally, Section 3.5 describes the model employed for the SEA pre-extrapolation of strain data and Section 3.6 is dedicated to the numerical model of the support system of the stabilizer, developed to reproduce the non-ideal boundary conditions observed during the tests.

3.1. Specimen and experimental setup

The structure under investigation in this work is a full-scale Medium Altitude Long Endurance (MALE) UAV composite aircraft stabilizer wing [78], whose displacement, strain and internal action fields are reconstructed through the iFEM. The stabilizer is composed of two main composite panels—hereafter referred to as upper and lower skins—connected by eight longitudinal half-stringers acting as internal stiffening elements. An overview of the stabilizer is provided in Fig. 8 and Fig. 9. It is worth noting that in Fig. 8 the stabilizer is shown in a vertical orientation due to laboratory constraints; however, in its actual operational configuration, it is mounted horizontally on the UAV structure.

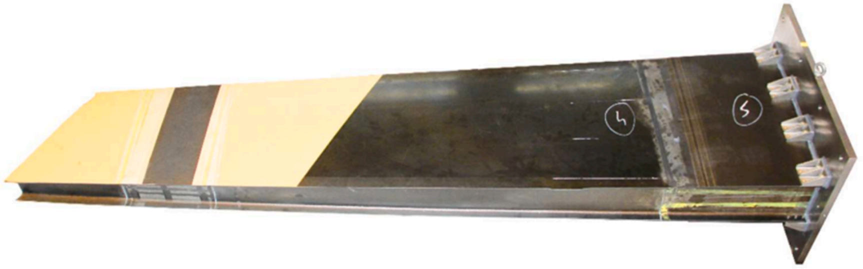

Fig. 9. Test sample and its supporting system (view from the lower skin side).

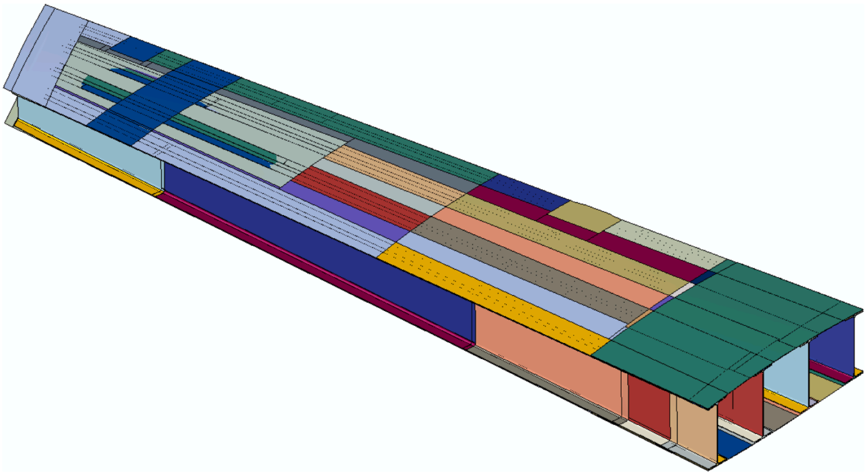

Fig. 10. Schematic distribution of ply orientations and thickness regions in the CAD model of the stabilizer.

This is a complex three-dimensional composite structure, approximately 3.3 m in length, with a total mass of about 35 kg. Both the thickness and the span of the cross-section vary along the longitudinal axis: the span ranges from a maximum of 0.9 m to a minimum of 0.48 m, while the thickness varies from a maximum of 0.22 m to a minimum of 0.12 m The skins are slightly curved and not flat, which contributes to the structural complexity. The entire stabilizer is fabricated from laminated composite materials, tailored for weight efficiency and mechanical performance. The skins present a variable thickness both longitudinally and transversally. Longitudinally, the thickness decreases from root to tip (left to right of Fig. 8), while transversally it increases in the areas where the stringers are bonded. The maximum skin thickness is approximately 7 mm, and the minimum is around 1.5 mm, obtained by stacking composite plies each 0.2 mm thick. Conversely, the stringers exhibit a constant thickness of 2 mm. A schematic view of the stabilizer highlighting all regions with different thicknesses and ply orientations is provided in Fig. 10, where such zones are distinguished using different colors. Due to confidentiality constraints, the exact thickness values of the individual structural components are not fully disclosed here. Other details of the demonstrator under investigation are reported in Fig. 11.

The stabilizer is mounted on a dedicated support system consisting of a triangular steel stand, a steel plate, and a total of eight aluminum brackets. The triangular steel stand ($E = 210000$ $[MPa]$, $\nu = 0.33$ $[-]$), serving as the primary load-bearing structure, is rigidly anchored to the ground by means of eight M24 bolts. It has a base footprint of 0.75 $m \times$ 1.050 m, a total height of 1.8 m, and incorporates two triangular stiffening plates that enhance its rigidity. All parts of the stand have a uniform thickness of 40 mm. Positioned between the stand and the stabilizer, the steel plate ($E = 210000$ $[MPa]$, $\nu = 0.33$ $[-]$) features a base surface of 0.65 $m \times$ 0.85 m, with the longer side oriented vertically in the assembly, and a uniform thickness of 30 mm. The plate is mechanically connected to the stand through ten M20 bolts. The stabilizer is connected to the steel plate through eight aluminum brackets ($E = 70000$ $[MPa]$, $\nu = 0.33$ $[-]$), each fastened to the plate by two M16 bolts and riveted to both the upper and lower skins of the stabilizer using six rivets per bracket. The brackets, measuring 0.050 $m \times$ 0.087 $m \times$ 0.110 m, are reinforced with three internal triangular stiffeners of 8 mm thickness to increase local rigidity.

The overall laboratory test rig is illustrated in Fig. 12, and the properties of the material used for the stabilizer are reported in Table 1.

The loading system comprises two MTS 244.11 hydraulic actuators (Fig. 13(a)), positioned approximately 2.7 m from the root section of the stabilizer. The actuators are equipped with load cells, which enable the force-controlled setting of the test bench [79]. The distance between the upper edge (leading edge) of the stabilizer and the application point of force F_1 is approximately 0.1 m, while the spacing between the two force application points (F_1 and F_2) is about 0.28 m, as shown in Fig. 13(c). The actuators apply out-of-plane forces—i.e., perpendicular to the surface of the stabilizer—through a custom-designed saddle system. Each saddle (Fig. 13(b)) is composed of two aluminum frames ($E = 70000$ $[MPa]$, $\nu = 0.33$ $[-]$) connected to the actuator rods via spherical hinges, and two wooden blocks ($E = 9000$ $[MPa]$, $\nu = 0.4$ $[-]$) that hold eight rubber pads.

These pads distribute the load uniformly onto the outer surfaces of the upper and lower skins, preventing local damage and mimicking realistic load transmission. Several loading scenarios were tested, and they are described in detail in Section 3.2. Additionally, dedicated displacement transducers were placed at the actuator contact zones to record the structural response in terms of deformation. These displacement measurements are essential for validating the accuracy of the iFEM algorithm, as they provide ground truth data against which the reconstructed displacements can be compared. The LUNA interrogation system includes internal referencing procedures that minimize thermal drift during the quasi-static tests, while the SEA pre-extrapolation

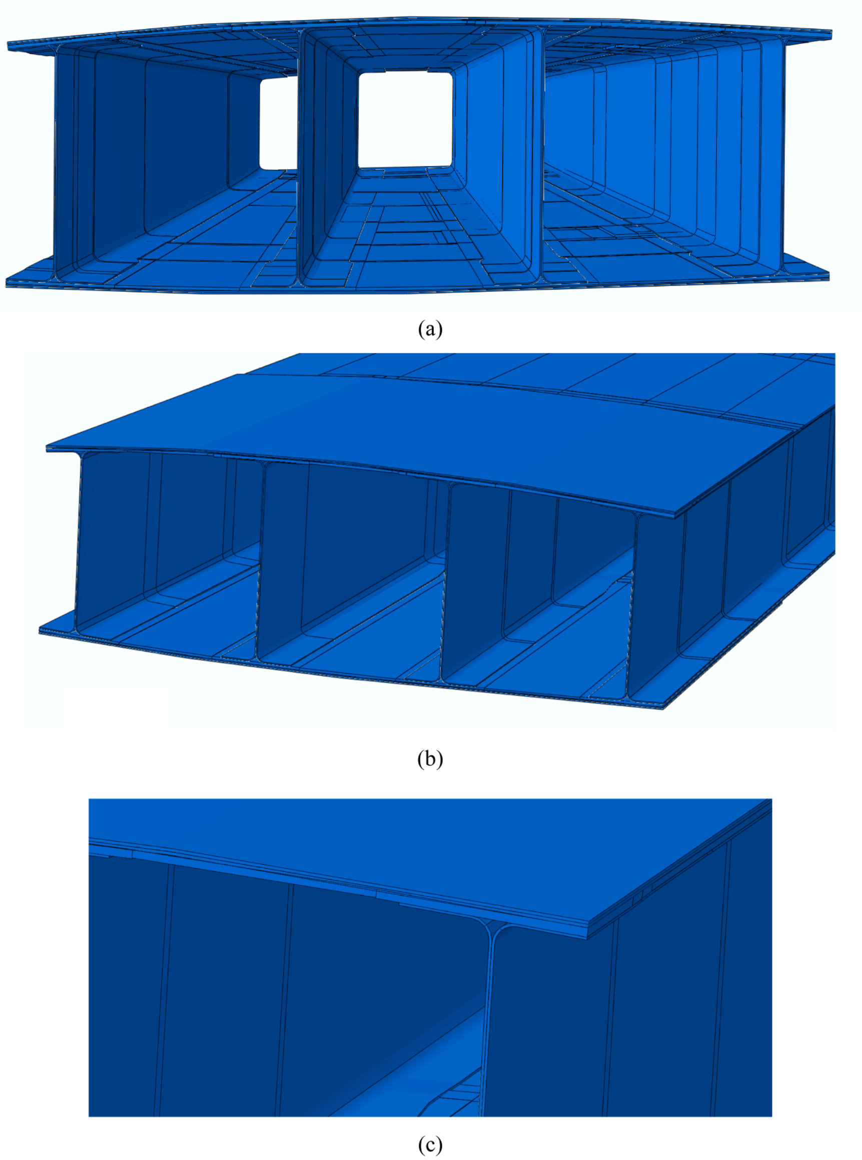
(a)

(b)

(c)

Fig. 11. Details of the stabilizer (from CAD modelling): (a) front view of the constrained side, (b) lateral view of the constrained side and (c) detail of the joint between a stringer and the skins.

provides additional smoothing of local noise before feeding the strain data into the iFEM framework.

3.2. Experimental quasi-static tests

To demonstrate the framework proposed in the present work, a series of static laboratory tests was conducted on the full-scale stabilizer specimen. The goal of these tests was to acquire distributed strain measurements, which serve as the essential input for the application of the iFEM strategy. These experimental activities were carried out using the setup previously described in Section 3.1, which was specifically designed to allow controlled and repeatable loading conditions.

A set of quasi-static load cases was defined, involving different combinations and magnitudes of the two external forces, denoted as F_1 and F_2. Each configuration was designed to explore a representative range of structural responses under different load distributions. The complete set of load cases, together with the corresponding measured displacements D_1 and D_2 at the actuator contact points, is reported in Table 3. In all tests, the hydraulic actuators were set up to apply tensile (pulling) loads to the stabilizer in a cantilever configuration, as schematically shown in Fig. 13(c). This loading arrangement induced bending in the component and, in some cases, also torsional effects.

For the purpose of demonstrating the present framework, only eight load cases from Table 2 were considered — specifically, cases 2, 4, 7, 8, 10, 14, 16, and 20. These were selected as they are representative of the overall loading conditions, capturing the range of bending- and torsion-dominated scenarios observed in the full dataset.

The actuators were force-controlled, with each actuator applying a load incrementally from 0 kN up to 8 kN in steps of 2 kN.

Each test consisted of the following steps (one example is shown in Fig. 14):

- a 30 s baseline with the actuators unloaded.
- A ramp to the nominal condition in 10 s.
- Static loading: 10 s (time window during which LUNA sensor readings were extracted and subsequently averaged).
- Unloading the structure: 10 s.
- A 30 s baseline with the structure unloaded.
- Repetitions from second to fifth point three times.

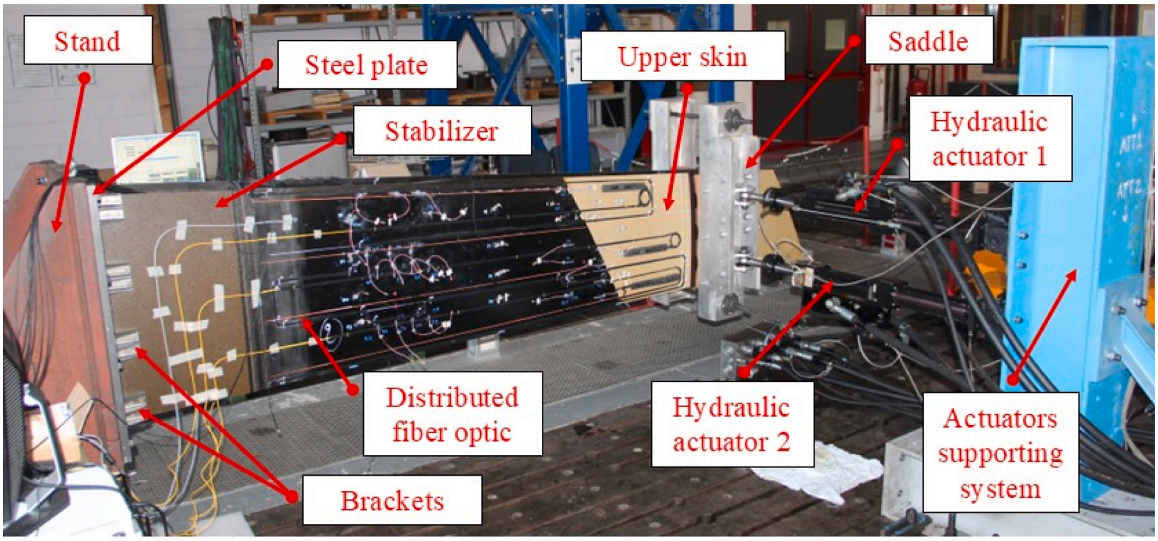

(a)

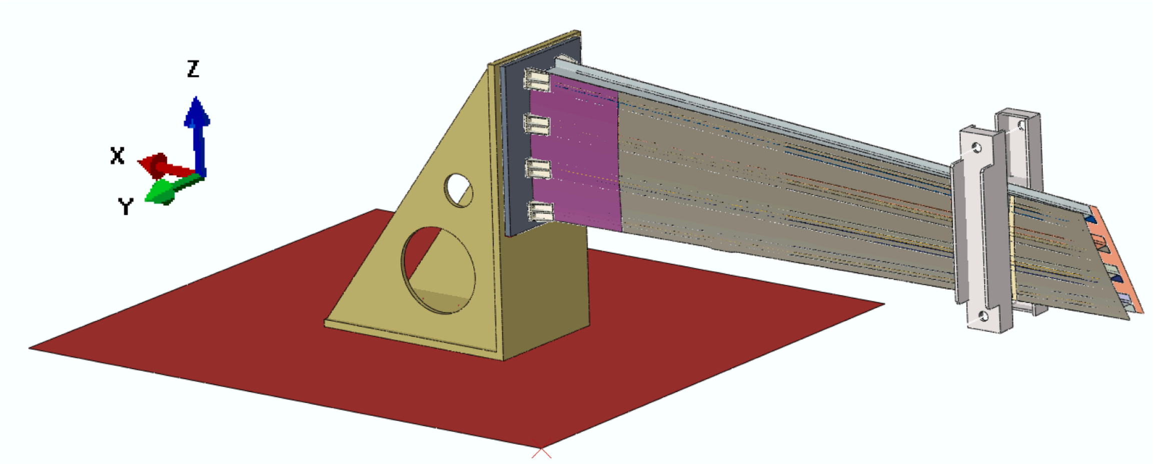

(b)

Fig. 12. Laboratory test rig for the experimental tests: (a) picture and (b) CAD model.

The temperature is assumed to be constant throughout the tests since the duration is about six minutes.

As previously mentioned, these displacement measures play a key role in the validation of the iFEM reconstruction strategy. Specifically, the displacements reconstructed by the iFEM algorithm—based solely on the input strain data acquired during the tests—will be directly compared against the experimentally measured displacements, thus providing a quantitative benchmark for evaluating the accuracy and reliability of the proposed approach.

3.3. The sensor network and its installation

Although the stabilizer was instrumented with various types of sensors—including Fiber Bragg Gratings (FBGs), temperature sensors (NTC thermistors), and others—for the purposes of the present study, only the LUNA distributed fiber optic sensors based on Optical Backscatter Reflectometry (OBR) are considered, as they were used to apply and validate the proposed framework.

The stabilizer structure is instrumented with 20 m of OBR fiber optic, which is interrogated using a LUNA ODiSI-B system. OBR is an interferometric technique capable of detecting local strain variations by analyzing the spectral characteristics of the light backscattered within the fiber. Unlike point sensors, this method enables continuous strain monitoring with extremely fine resolution, making it well-suited for SHM applications. This setup enables the acquisition of distributed strain measurements along the entire length of the fiber, with a spatial resolution of approximately one data point every 2.5 mm. This acquisition system allows for high-resolution monitoring of the strain field across the structure.

The layout of the fiber on the stabilizer is presented in Fig. 15 for the lower and upper skins, highlighting the areas covered by the sensing network.

The fiber is installed exclusively on the external surfaces of both skins, as the inner sides are not accessible due to structural constraints. The fiber follows four main rectilinear paths aligned with the longitudinal direction of the stabilizer. Only the strain data collected along these straight segments are considered valid for analysis, while those acquired in the corner regions—where the fiber bends—are discarded due to signal unreliability and ambiguous strain orientation.

The stringers are not equipped with sensors, except for a single fiber segment applied to each of the two external stringers. These segments are used solely to ensure continuity of the sensing path, allowing the fiber to pass from one skin to the other. Despite the high density of data—amounting to approximately 6500 strain measurements—it is evident from Fig. 15 that the spatial coverage is limited relative to the overall dimensions and complexity of the structure. In particular, the

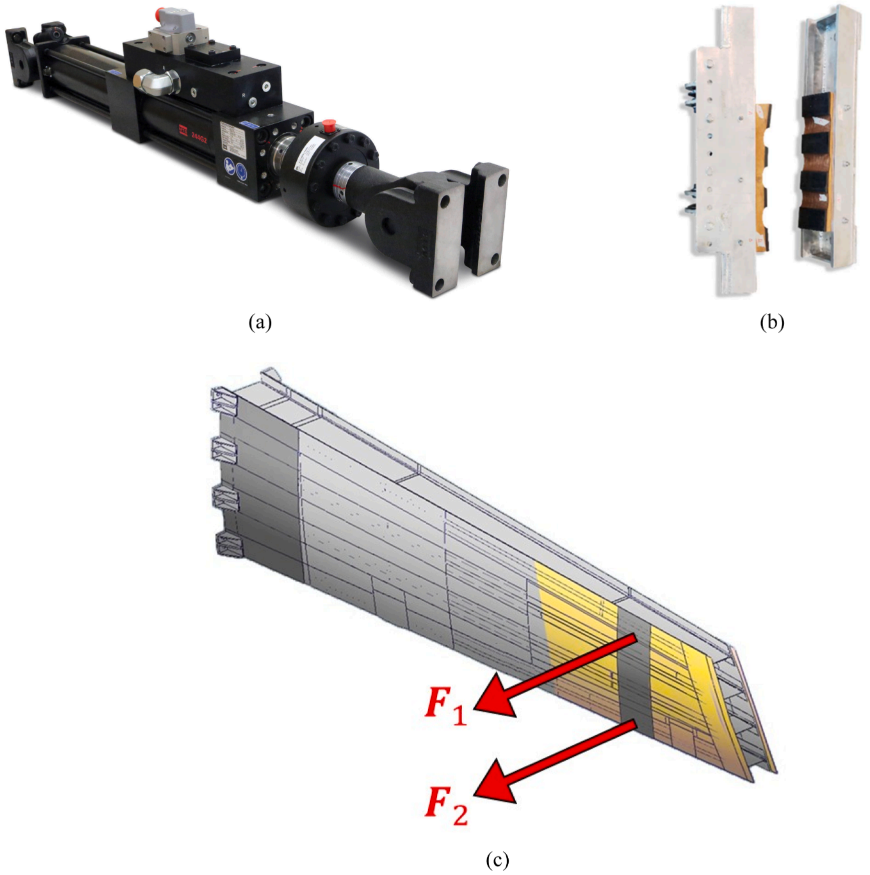

(a) (b)

(c)

Fig. 13. (a) MTS 244.11 hydraulic actuator, (b) saddle that transfers their loads to the structure and (c) application points of the actuator loads. Same reference system of Fig. 12.

Table 2
Material properties of the stabilizer's composite structure, as provided by the manufacturer.

Cytec 977–2–34–24KIMS-196-T1					
E_{11} $[MPa]$	E_{22} = E_{33} $[MPa]$	υ_{12} = υ_{13} $[-]$	υ_{23} $[-]$	G_{12} = G_{13} $[MPa]$	G_{23} $[MPa]$
125,000	7575	0.34	0.55	3150	2720

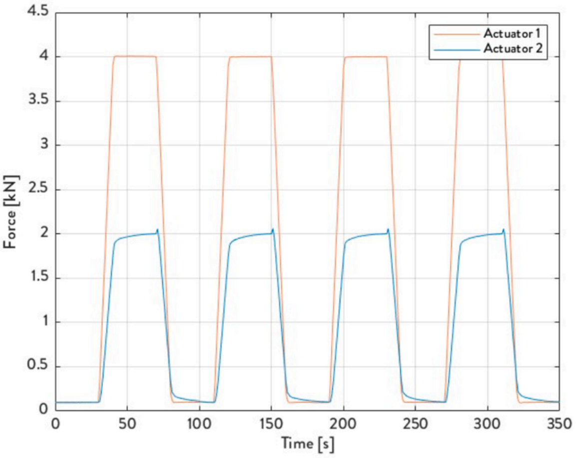

Fig. 14. Load time series for the load case 9 of Table 3.

fiber is applied only in the central region of each skin, leaving both ends entirely unsensorized. Moreover, the presence of varying skin thickness adds an additional layer of complexity to the interpretation of strain data, as the strain state is influenced by local stiffness variations.

This setup notably differs from the idealized sensing configuration introduced in Section 2.3, where each measurement point is composed of a top/bottom pair of strain gauge rosettes capable of capturing all three in-plane strain components. In contrast, the optical fiber provides only the strain component along its own axis—that is, the fiber's longitudinal direction—which, depending on the orientation of each segment, corresponds either to the longitudinal strain ε_{xx} or the transverse strain ε_{yy} in the structure. As illustrated in Fig. 15, most of the recorded strain data correspond to ε_{xx}, with only a limited number of segments aligned transversely and thus capable of capturing ε_{yy}. The in-plane shear strain component γ_{xy} cannot be measured with this acquisition method.

The design of the sensor network was the result of a preliminary multidisciplinary effort aimed at balancing monitoring accuracy, physical feasibility, and implementation constraints. Rather than relying on a purely theoretical optimization, the sensor layout was developed through collaboration between the research team, the stabilizer manufacturer, and fiber optic sensing specialists. This process integrated prior numerical insights—such as finite element predictions of strain distribution under representative loading conditions—with practical experience and technical considerations specific to fiber optic systems.

Several physical and engineering criteria guided the layout definition, including the need to:

- avoid sharp directional changes to reduce the risk of signal degradation or fiber damage.

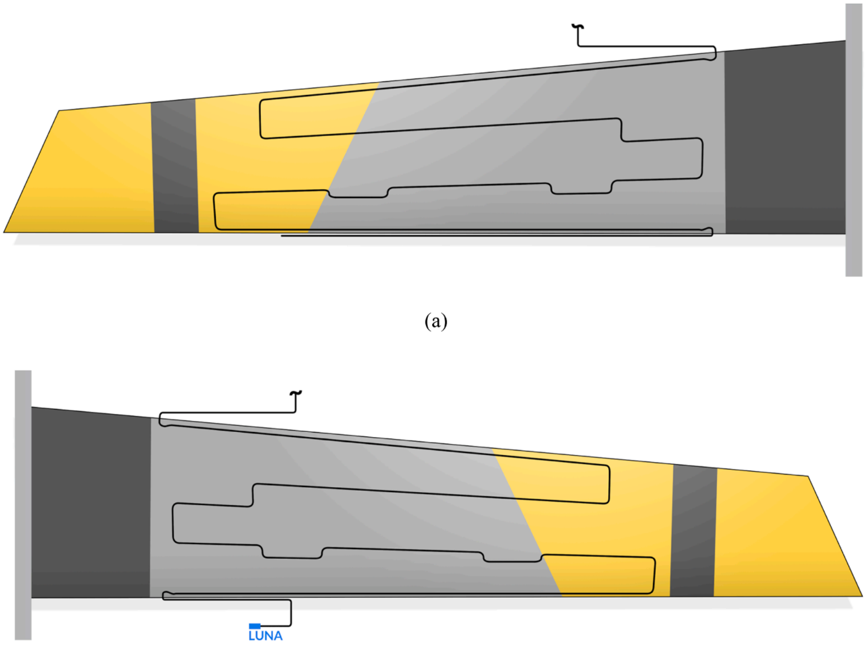

(a)

(b)

Fig. 15. Distributed fiber optic distribution on the stabilizer skin: (a) upper and (b) lower.

- Avoid overlapping with other sensors installed on the demonstrator.
- Minimize unintended load transfer through the fiber, which could compromise measurement accuracy.
- Maximize straight segments to ensure consistent acquisition directions and facilitate interpretation.
- Provide strain data in both longitudinal and transverse directions to support robust biaxial field reconstruction.
- Leave adequate clearance between the fiber paths and the impact points designated for future dynamic tests, to prevent potential damage during post-static testing phases.
- Avoid placing measurement points at discontinuities—e.g., abrupt changes in thickness—to reduce noise and improve data reliability.

Furthermore, constraints related to the manufacturing process and stabilizer geometry—such as curvature, accessibility, and manual placement limitations—were carefully considered. Although the final configuration is not the outcome of a formal optimization algorithm, it represents a technically robust and practically viable solution, as confirmed by the high quality of the strain measurements and the reliable results obtained through the iFEM reconstructions discussed in the following sections.

Before installing the sensor, the surface of the vessel was meticulously prepared to ensure optimal adhesion and, consequently, accurate signal acquisition. The preparation process included an initial sanding phase, followed by a thorough cleaning using acetone to remove any residual contaminants. The optical fiber was then manually positioned onto the specimen's surface and temporarily held in place with paper tape to allow for precise alignment. Once the entire fiber was correctly

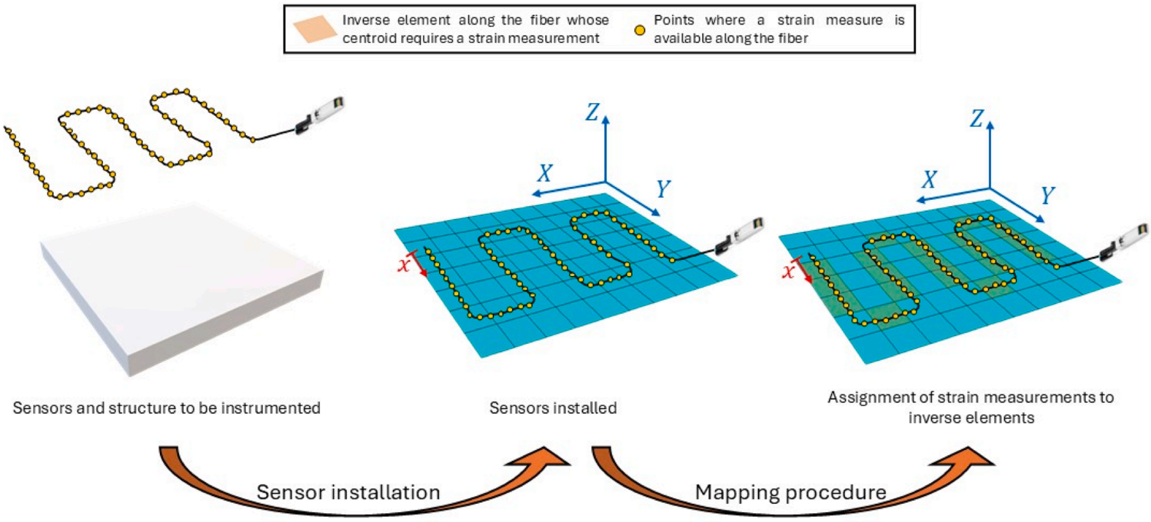

Fig. 16. Schematic representation of the mapping procedure used to associate fiber-optic strain measurements with specific physical locations on the surface of a representative plate. The yellow dots indicate all available measurement points along the fiber, while the highlighted elements correspond to those requiring strain input at their centroids. For each element, the nearest yellow point was selected and used as the input measurement. Adapted from [72] with permission.

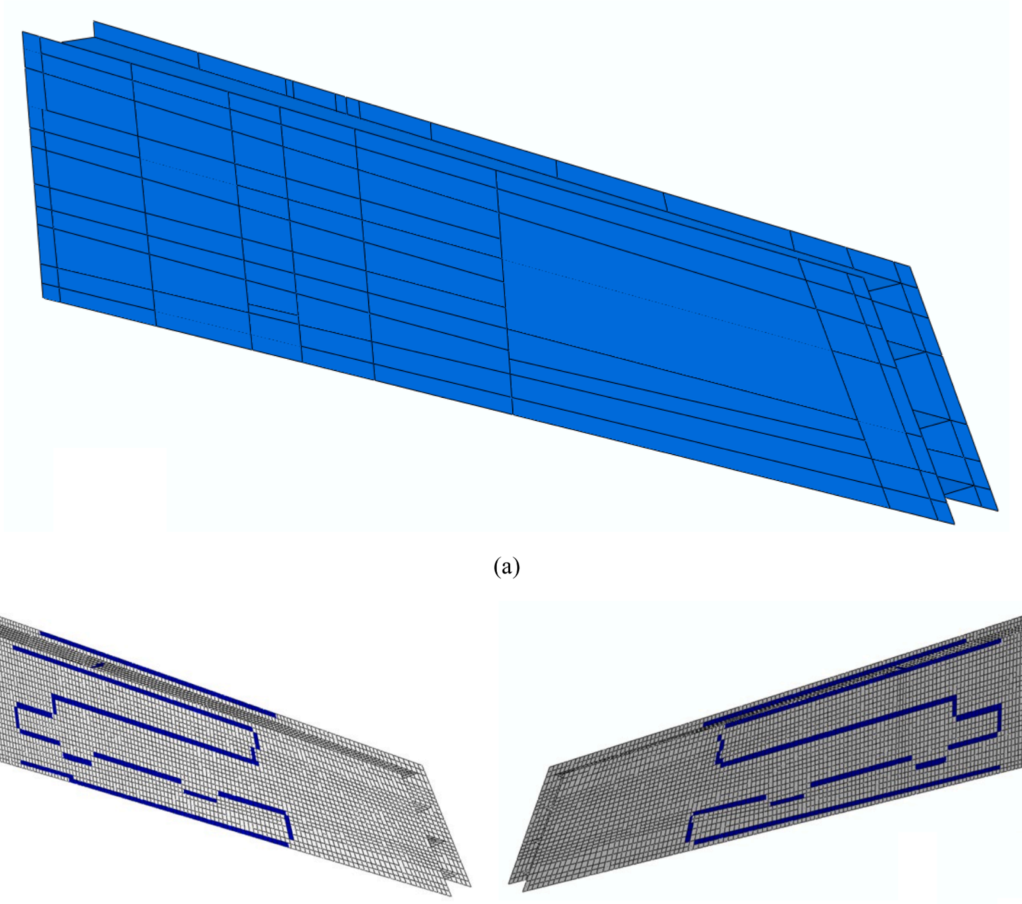

(a)

(b)

(c)

Fig. 17. Inverse FE model in ABAQUS CAE: (a) assembly 3D view with BCs, (b) iQS4 mesh for the upper side and (c) iQS4 mesh for the lower side. The elements of the inverse mesh with strain measures are highlighted in blue.

laid out, a mapping procedure was carried out to correlate the sensor's internal measurement reference with actual physical locations on the structure. This step—schematically illustrated in Fig. 16—was essential for accurately converting the distance from the fiber connector (as registered by the control unit) into corresponding spatial coordinates on the specimen. As shown in the representative example in Fig. 16, the discrete measurement points along the fiber (marked as yellow dots) were associated with the centroids of the inverse elements that required strain input. For each of these inverse elements, the nearest available measurement point was selected and used in the inverse reconstruction process. This concept will become clearer in the following section, where the inverse model and its implementation are described in detail.

Following the mapping phase, the sensor was permanently bonded to the surface using 3M® DP490 epoxy structural adhesive. This adhesive step was critical to ensure consistent strain transfer from the structure to the sensor. Careful application was necessary to avoid excessive adhesive thickness, which could introduce measurement artifacts and compromise accuracy. Finally, to protect the fiber at critical transition zones—particularly at the entry point of the fiber and at the transition from the external to the internal surface—a rubber heat-shrink tube was applied. This provided mechanical protection without interfering with the sensor's function.

A pre-processing step required by the iFEM model involves filtering the strain data acquired from the experimental sensor network, to reduce noise and obtain clean, reliable strain values. This filtering was carried out using a Butterworth filter with a cutoff frequency of 0.1 Hz. In addition to noise reduction, the dataset was also processed to remove outliers, ensuring the consistency and physical plausibility of the strain measurements. The sampling frequency adopted for the LUNA acquisitions was 10 Hz, while that of the actuators was set to 100 Hz.

3.4. *The iFEM model*

To build the inverse model of the stabilizer, the structure must be entirely modeled using iQS4 shell elements, as explained in Section 2. This constraint represents a first simplification compared to the high-fidelity CAD model of Fig. 11. An additional simplification lies in the modeling strategy: the entire stabilizer is represented as a single part, meaning that the connections between stringers and skins are treated as simple welded intersections. Furthermore, although the stabilizer does not feature perfectly flat skins, they are approximated as planar surfaces in the inverse model to simplify the geometry. However, this curvature is sufficiently small, and it does not significantly influence overall structural behavior and results. Fig. 17(a) shows the complete iFEM model of the stabilizer made in ABAQUS CAE environment, with the simplifications described above, along with the shell mesh adopted for its discretization. The average element size is 25 mm, resulting in a total of 10,450 iQS4 elements and approximately 27,500 nodes, which represents a relatively fine discretization suitable for the purposes of this study. The resulting mesh size limits the computational time within acceptable bounds in view of real-time applications and allows the input strain field definition from experimental measures in all the elements intersected by the optical fiber. Strain measurements from experimental tests, as described in Section 3.2, are mapped onto this mesh based on

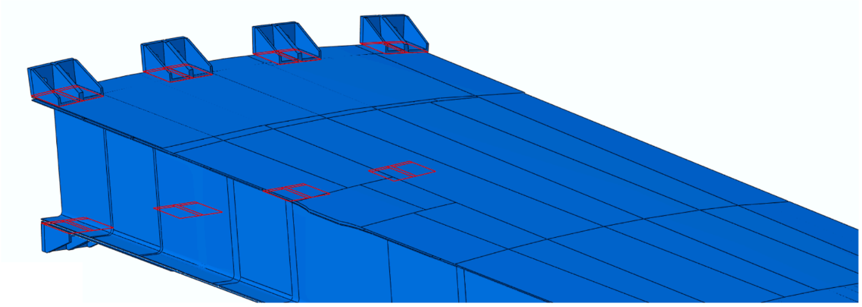

Fig. 18. Portions of the stabilizer where fully clamp boundary conditions were applied to the inverse model.

their global coordinates. The outcome of this mapping is illustrated in Fig. 17(b) and (c), where elements containing assigned strain measurements are highlighted in blue as consistent with Fig. 15. Following the standard iFEM practice, unit weighting factors were assigned to the strain components directly measured by the fiber optic sensors, whereas reduced coefficients of 10^{-4} were used for the unmeasured components to minimize their influence on the least-squares functional. This weighting scheme ensures numerical stability and accuracy even in regions with sparse sensor coverage.

It can be observed that the sensor network is rather limited in coverage relative to the overall structure, as most of the elements do not contain any strain measurements. For this reason, the SEA pre-extrapolation of the strain field must be applied, making use of the formulation recalled in Section 2.3. The structural model adopted for the SEA pre-extrapolation procedure is described in detail in the following Section 3.4.

A fundamental aspect of the present work lies in the accurate identification of the real boundary conditions acting on the stabilizer, to ensure reliable displacement and strain field reconstructions using the iFEM. Indeed, the accuracy of the iFEM results is highly sensitive to the imposed constraints, and even slight deviations from the actual support behavior can significantly affect the quality of the reconstruction.

As a first modeling assumption, ideal clamped boundary conditions were imposed in the iFEM model at the locations where the stabilizer is connected to the eight steel brackets. These idealized constraints represent a fully fixed support, neglecting any local compliance or flexibility at the bracket interfaces. The surfaces of the model where these ideal boundary conditions are applied are highlighted in Fig. 18. In the following paragraph, the sources of uncertainty in defining the appropriate boundary conditions for the structure under investigation are described, based on the experimental setup.

3.5. *Uncertainty in the boundary conditions*

At the end of the experimental campaigns, it became evident that a more detailed analysis of the sources of uncertainty in the stabilizer's boundary conditions, provided by the support system of the stabilizer, was necessary. Two main aspects to study were identified: the deformability of the individual components of the support system, and the compliance at the interfaces between these components. These two factors introduce small but non-negligible displacements and rotations at the connection points, effectively altering the boundary conditions initially assumed as ideal. As a result, ideal constraints in the iFEM model may no longer accurately reflect the actual support behavior, thereby degrading the quality of the displacement and strain field reconstruction.

The sources of uncertainty affecting the boundary conditions of the stabilizer due to the support system are summarized in Table 4. In this table, for each item, the actual type of physical connection is indicated, along with an assessment of whether its influence can be considered negligible or not. This latter evaluation was carried out experimentally using a laser displacement measurement system, which allowed for the detection of small relative displacements of each component of the support system. Through this process, it was possible to determine whether each source of uncertainty could be safely disregarded or should be accounted for in the iFEM modeling phase.

Table 4
Identified sources of uncertainty affecting the boundary conditions of the stabilizer.

N°	Item	Actual joint type	Can be neglected?
1	Ground deformability	–	Yes
2	Compliance of the triangular steel stand-to-ground interface	Eight M24 bolts	Yes
3	Steel stand deformability	–	Yes
4	Compliance of the triangular stand-to- steel plate interface	Ten M20 bolts	Yes
5	Steel plate deformability	–	Yes
6	Compliance of steel plate-to-aluminum brackets interface	Two M16 bolts (for each bracket)	No
7	Aluminum brackets deformability	–	No
8	Compliance of brackets-to-stabilizer interface	Six rivets (for each bracket)	Yes

Fig. 19. Detail of the mechanical connection bracket-stabilizer (rivets) and bracket-steel plate (bolts).

As shown in Table 4, the only two contributions that cannot be considered negligible are the compliance of the steel plate–bracket connection and the compliance of the brackets themselves (see Fig. 19). These effects imply that the stabilizer is no longer subjected to a fully clamped (ideal) constraint, but rather to a non-ideal boundary condition. In particular, the local flexibility of the brackets and the connection between them and the steel plate led to small but significant rotations and displacements at the nodes where the brackets are connected to the stabilizer. These generalized displacements must be imposed as boundary conditions in the updated iFEM model of the stabilizer to improve the accuracy of the reconstruction.

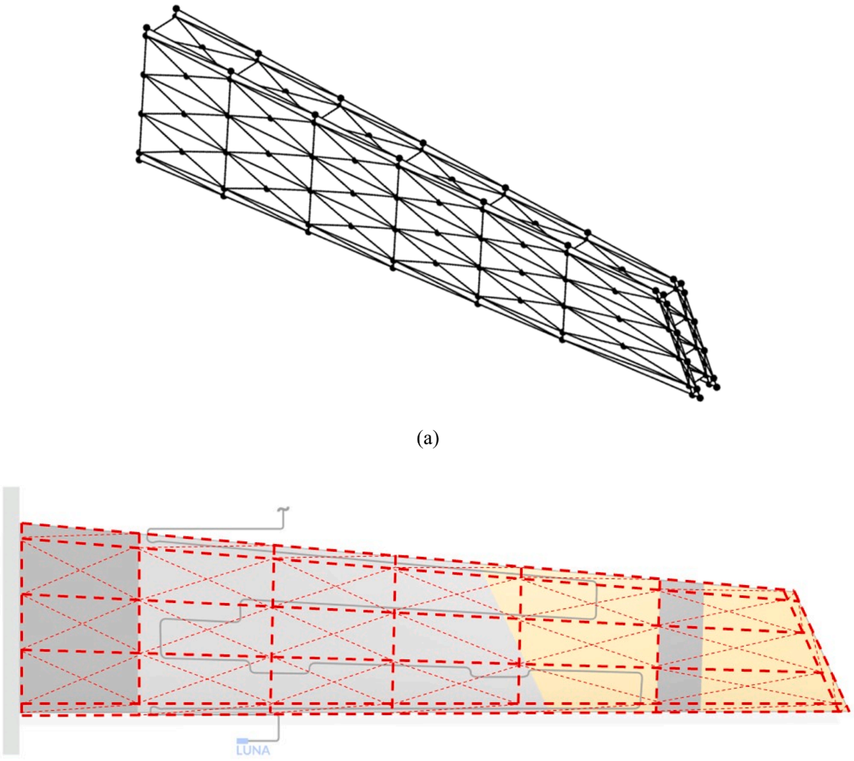

(a)

(b)

Fig. 20. Mesh of the stabilizer structure used for the application of SEA pre-extrapolation: (a) cross-pattern 3D view and (b) mesh overlaid on the upper skin of the stabilizer. Same reference system of Fig. 12.

To compute these generalized displacements—i.e., nodal translations and rotations—a dedicated static FE model of the support system must be developed. In this model, the brackets are treated as deformable components, and the loads reconstructed by the iFEM under the ideal clamped assumption are applied at the stabilizer's root section. The procedure used to extract such equivalent loads is the same as the one described in Section 2.4.

This approach is necessary because, in real-world applications—unlike controlled experimental setups—the actual external loads acting on the structure are generally unknown. Consequently, the iFEM reconstruction, assuming ideal clamped boundary conditions serves as a first step to estimate the internal forces at the clamping section. These reconstructed internal actions are then applied to the finite element model of the support system, allowing the calculation of the displacements and rotations induced by the deformability of the brackets. Finally, these computed quantities are imposed as boundary conditions in a new iFEM model, thus accounting for non-ideal support conditions and enabling a more realistic reconstruction of the stabilizer's structural response. The numerical model of the support system used to carry out this procedure is presented and described in detail in Section 3.6.

3.6. Stabilizer model for SEA pre-extrapolation

As anticipated before, sensors application on the whole structure is practically unfeasible. A pre-extrapolation procedure is then used to obtain strain data in the elements free from any measurement input to improve the reconstruction's accuracy. As already anticipated, the SEA method is used in this work for the pre-extrapolation of the input measures

Even though the SEA method is formulated for a two-dimensional domain, the algorithm described in Section 2.3 can also be applied to a three-dimensional structure. When the structure is composed of several planar surfaces with different orientations, each triangular mesh element is locally defined in the (x, y) reference system of the plane it belongs to (see Fig. 4). In this way, while the formulation of each element remains bi-dimensional, all the degrees of freedom—representing the strain field—are assembled into a global system that captures the behavior of the full three-dimensional structure.

In the most general case, a total of four independent extrapolations is required for each iFEM simulation: the strain (i) along and (ii) transversal to the load direction on both the (a) top and (b) bottom side of each surface that defines the three-dimensional structure. As already explained in the methodology section, assuming a membrane-dominated behavior, internal and external strain values are considered equal, which is a reasonable simplification for the purpose of this study. Apart from this, the number of SEA elements must be tuned according to the problem under analysis, considering the input strain measure density within the domain. As a rule of thumb, a high number of input data requires a finer mesh. However, since four independent SEA must be executed for each iFEM analysis, limiting the number of elements, and thus the computational burden, is also a primary concern. For the present case, the triangular mesh adopted is the one shown in Fig. 20. It is important to note that this SEA mesh is implemented on the same geometry described and illustrated in Fig. 17(a). A cross-pattern triangular configuration was selected, resulting in a total of 476 triangular elements.

The SEA mesh refinement was selected based on preliminary numerical trials, which indicated that increasing mesh density beyond a certain threshold produced negligible accuracy gains while increasing computational effort. Both structured triangular and cross-pattern discretizations were tested, yielding comparable reconstruction accuracy. Consistently with observations reported in [62], the cross-pattern discretization proved particularly efficient in capturing the anisotropic strain field of the stabilizer with a reduced number of elements.

In many real structural configurations, including the one considered in this study, an additional complication arises: some of the planar

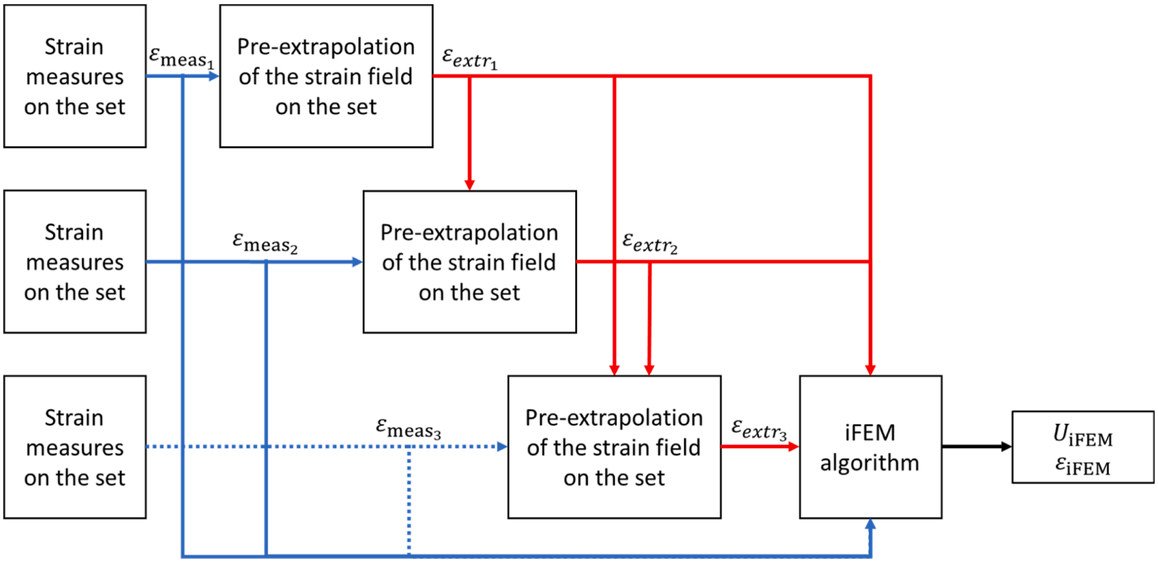

Fig. 21. Scheme of the iFEM steps with the pre-extrapolation procedure for complex 3D structures.

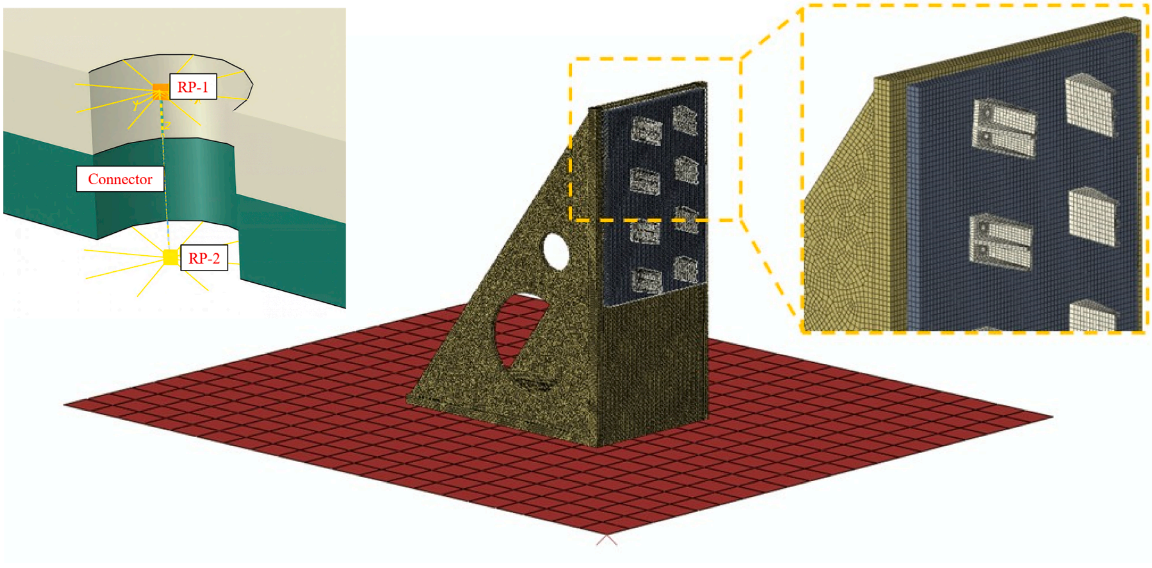

Fig. 22. Numerical FE model of the support system of the stabilizer with a detail of the brackets.

regions where SEA pre-extrapolation is required do not contain any strain sensors. Such is the case, for example, of longitudinal stringers. To solve this challenge, the proposed strategy consists in performing the SEA pre-extrapolation in sequential steps, each one corresponding to a specific portion of the structure (i.e., a set). The selected sequence for this case study—lower skin, upper skin, and longitudinal stringers—follows the principle that planar regions with available strain measurements must be processed first, allowing extrapolation to be propagated toward regions without sensors, such as the stringers. At each step, the strain field is fitted using:

- the strain measurements from sensors located on the current set.
- The strain values already extrapolated on previous sets at nodes shared with the current one.

This sequential process enables the estimation of the strain field even in regions without any strain sensors, provided that these regions are positioned at the end of the pre-extrapolation sequence. Fig. 21 illustrates a schematic of the multi-step algorithm in combination with iFEM, considering a representative case with three sets. The third set, which lacks direct sensor input, is highlighted with dashed lines to emphasize that reliable extrapolation is still achievable by enforcing continuity with the strain fields reconstructed in the previously processed sets.

3.7. Numerical model of the support system of the stabilizer

The finite element model made in ABAQUS CAE used to represent the support system of the stabilizer—and thus to simulate the actual, non-ideal constraint conditions acting on the stabilizer structure—is shown in Fig. 22. The constraint conditions applied in this model are defined to reflect the actual behavior of the support system observed in the laboratory with the details presented in Table 4.

In particular, the FE model of support system comprises: a triangular steel stand, connected to a floor plate, a rectangular steel plate and finally eight aluminum brackets. The geometry of these components has already been described in a previous section; therefore, the following focuses directly on the adopted modeling strategies.

From a numerical point of view, the connection between the stand

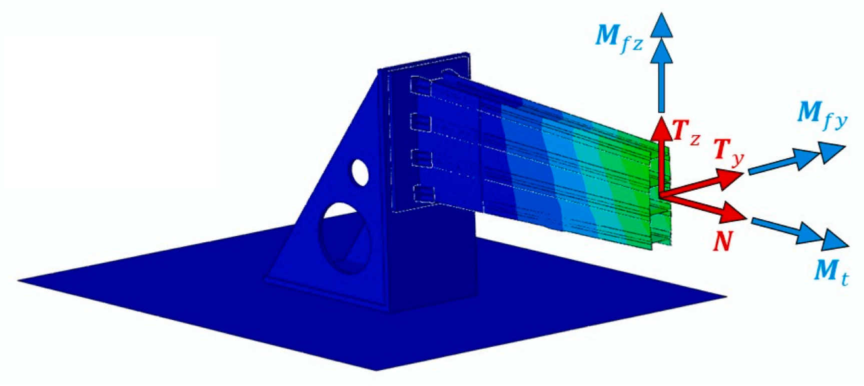

Fig. 23. Example of internal forces to which a generic cross-section of the stabilizer can generally be subjected: forces ($\boldsymbol{T_z}$, $\boldsymbol{T_y}$ and $\boldsymbol{N}$) and moments ($\boldsymbol{M_{fz}}$, $\boldsymbol{M_{fy}}$ and $\boldsymbol{M_t}$).

and both the ground and the steel plate is modeled using tie constraints. The stand structure was discretized in ABAQUS using 35,600 solid elements of type C3D8R. Furthermore, the floor is modeled as a rigid surface, which is fully fixed, representing an infinitely stiff foundation with no deformation under load.

Moving on to the steel plate, it is connected to the triangular stand through a tie constraint, which is intended to simulate the mechanical effect of ten M20 bolts. This component was also discretized in ABAQUS using 1800 solid elements of type C3D8R and the total weight registered is 120 kg.

Finally, the model includes eight aluminum brackets that connect the stabilizer to the overall support system structure. Each bracket is discretized using a total of 200 solid elements of type C3D8R. This component plays a critical role in the overall mechanical behavior of the support system, as its flexibility, along with its connection to the steel plate, introduces non-negligible deviations from ideal clamped boundary conditions. These deviations have been found to significantly affect the accuracy of the iFEM-based reconstruction strategy and must therefore be properly accounted for in the modeling process.

The M16 bolts used to connect each bracket to the steel plate are modeled as preloaded bolts by means of a translator element connector (Fig. 22 on the left) [80]. This approach treats the bolt as a digital spring acting along its axis, allowing the application of preload either as an axial force or as an imposed length change. While it does not explicitly represent the bolt's solid geometry, local stress concentrations, or joint friction, it efficiently captures the global preload effect and is sufficient for the purposes of the present framework. One end of the bolt is pinned to the steel plate, and the other one liked with a multi-point constraint to the nut contact area on each bracket. A surface-to-surface contact is created between the steel plate and the brackets. The friction coefficient is set to 0.1 based on preliminary calibration tests. Finally, the bolt pre-load is applied with a value of 18 kN.

Importantly, the fidelity of this numerical model was validated through comparison with experimental displacements measured via laser-based acquisition systems. These measurements confirmed that the support structure, specifically the brackets and their connections to the steel plate, introduce slight flexibility effects that influence the overall iFEM reconstruction of the stabilizer. The constraint conditions and the level of detail included in the model—such as the representation of bolts, contacts, and tie constraints—were thus calibrated to reproduce this behavior as closely as possible.

Finally, all the material properties adopted in the model are consistent with those already detailed in Section 3.1. It is also important to highlight that the mechanical behavior of all components was assumed to be linear elastic, in line with the small deformation regime observed during the experimental campaign and consistent with the assumptions made in the iFEM formulation.

Table 3

Summary of all the experimental tests with different combinations of the loads provided by the actuators and related displacements.

Load case	F_1 $[kN]$	F_2 $[kN]$	D_1 $[mm]$	D_2 $[mm]$
1	2	0	4.30	2.94
2	2	2	7.25	6.84
3	2	4	10.49	10.31
4	2	6	13.78	14.26
5	2	8	17.18	18.26
6	4	0	8.96	6.12
7	4	2	11.96	9.71
8	4	4	15.25	14.66
9	4	6	18.60	17.68
10	4	8	22.10	21.80
11	6	0	13.66	9.36
12	6	2	16.59	12.91
13	6	4	20.15	17.13
14	6	6	23.58	22.26
15	6	8	27.21	25.45
16	8	0	18.58	12.96
17	8	2	21.82	16.63
18	8	4	25.25	20.85
19	8	6	28.88	25.06
20	8	8	32.52	30.28

The most critical feature of the present static FE model is the implementation of internal actions reconstructed via the iFEM methodology. These actions are applied to evaluate the displacements and rotations that should be imposed as generalized boundary conditions on the iFEM model of the stabilizer alone. This approach allows the effects of non-ideal constraints to be considered, thus improving the reconstruction accuracy compared to the case of idealized clamped conditions. The internal actions are evaluated for simplicity at the root cross-section of the stabilizer.

The results of the internal action reconstruction through the procedure of Section 2.4 were also cross validated using the in-built section analysis tool in ABAQUS CAE. At the given section, six generalized internal actions (three force components and three moment components) are theoretically transmitted, as illustrated in Fig. 23. Depending on the specific load configuration applied to the structure, some of these components may dominate while others may be negligible.

In the present case, all the relevant internal actions of the specific load case scenario are imposed on the floor–stand–plate–brackets support system through a kinematic coupling constraint, with the reference node located vertically at the centroid of the considered stabilizer cross-section and horizontally at the mid-width section of the brackets (Fig. 18).

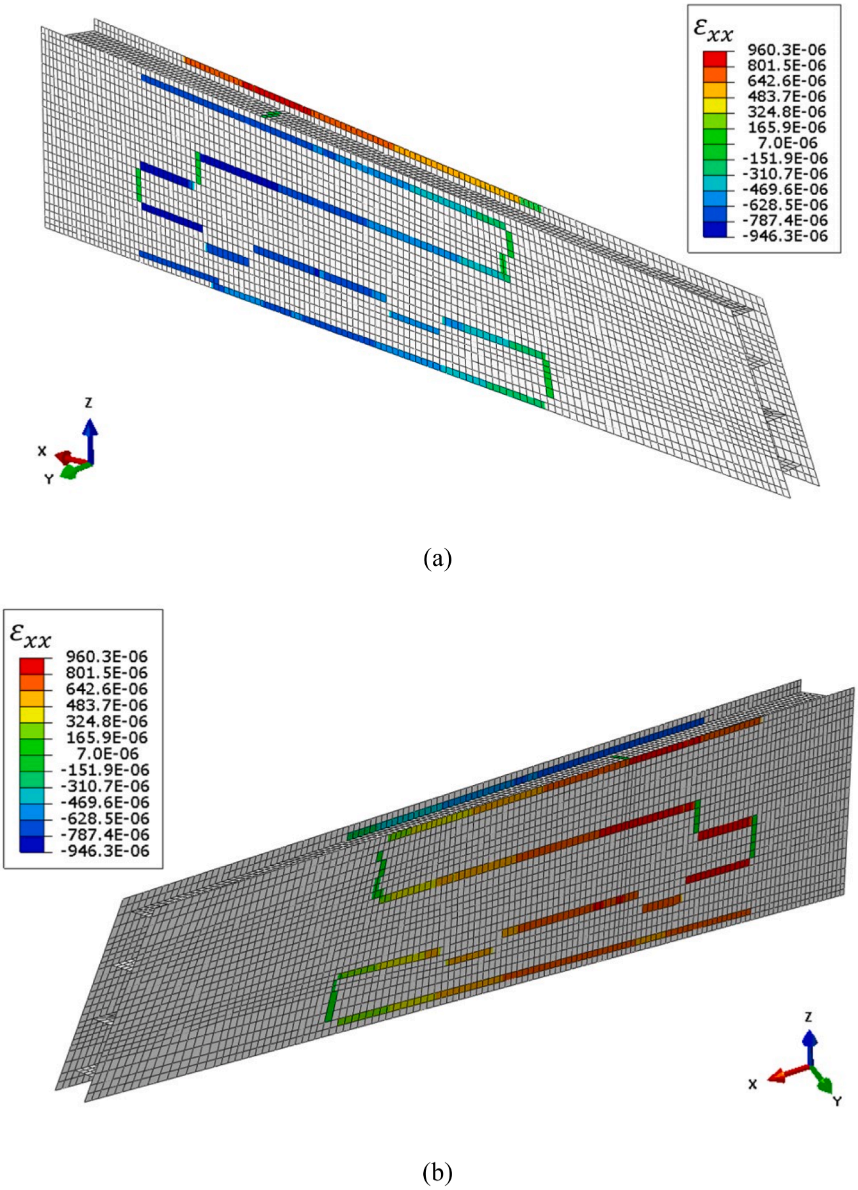

Fig. 24. Longitudinal strain measures $\boldsymbol{\varepsilon_{xx}}$ of the sensor network for the load case n°14 (unit of measurement: [με]): (a) upper skin side view and (b) lower skin side view.

4. Results and discussion

For the discussion of the results obtained, reference is made to load case No 14 (bending) and No 16 (torsion) of Table 3, while complete results for all load cases are reported in the tables.

4.1. Input strain and SEA-based pre-extrapolation

For load case number 14, Fig. 24 and Fig. 25 show the longitudinal and transversal strain measurements (ε_{xx} and ε_{yy}) obtained from the experimental test and pre-processed according to the procedure described in Section 2.3, as recorded by the sensor network. Specifically, the two figures refer to the measurements on the upper and lower skins on the outer side, where the distributed optical fiber is actually installed (the same applies to the fiber segments mounted on the outer side of the lateral stringers).

This detail is relevant because, as anticipated in the methodological section, assuming membrane-dominated behavior, internal and external strain values are considered equal (i.e., $\varepsilon^{+} = \varepsilon^{-}$), which is a reasonable simplification for the purposes of this study. Therefore, internal-side strain measurements are not reported, as they follow the previous assumption. As can clearly be observed, since this is a bending-dominated case, the longitudinal strains are significantly higher in magnitude than the transversal ones, and their absolute value decreases progressively with the distance from the clamped edge, reflecting the expected deformation pattern. It can also be noticed that the number of sensors in the transversal direction is extremely limited, which makes the reconstruction particularly challenging, especially in torsion-dominated cases. To avoid overloading the discussion, only the experimental strain data for case 14 is reported in this section. Care must be taken when interpreting these figures. For example, in Fig. 25(a), transversal strain values appear along the longitudinal segments of the fiber; however, these values are actually zero.

As already discussed in the case study and sensor network description, although the number of measurement points along the optical fiber is relatively high, it is still limited with respect to the overall extent of the structure. For this reason, a pre-extrapolation step is required. The results obtained for the SEA strain in the pre-extrapolation stage, for

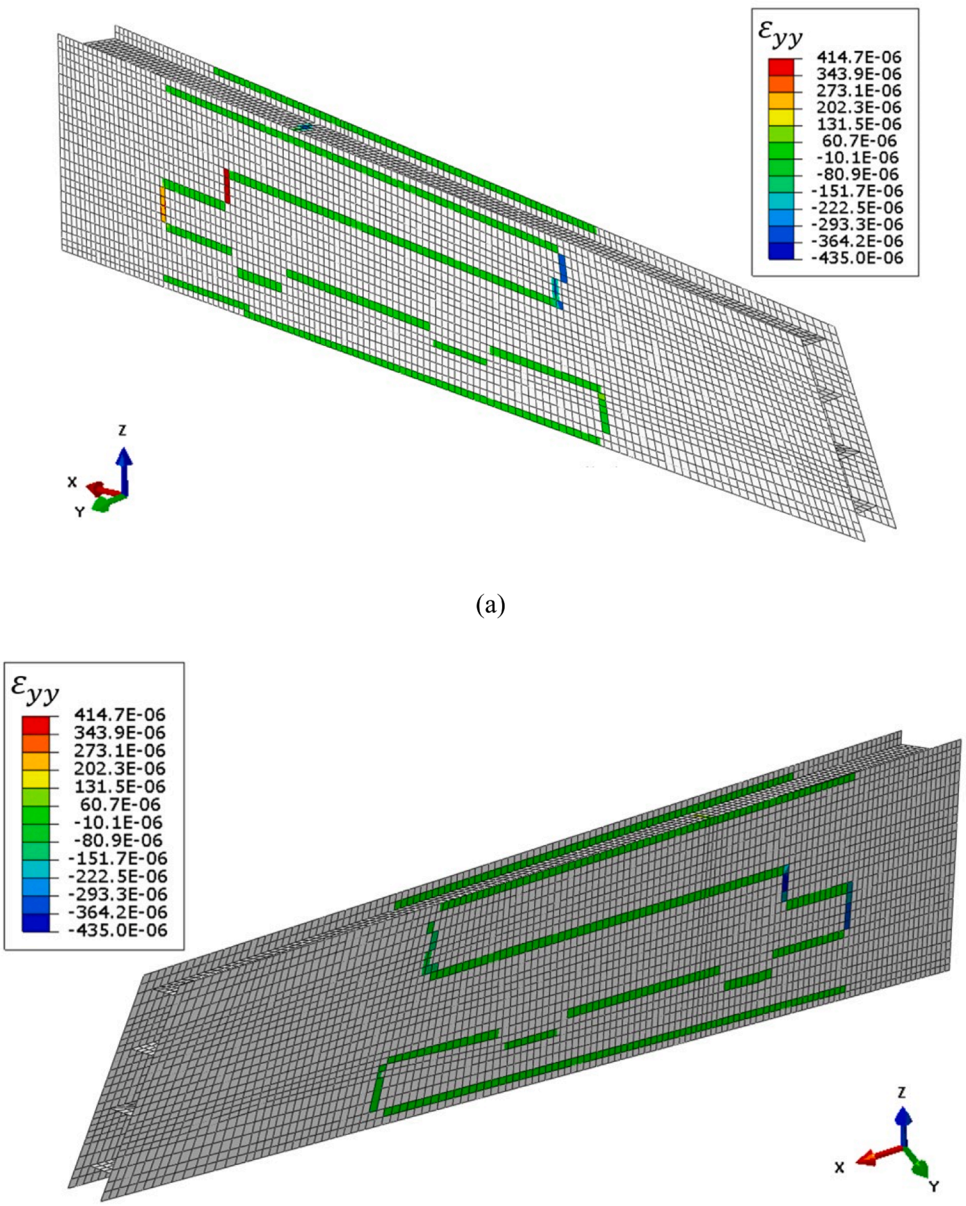

(a)

(b)

Fig. 25. Transversal strain measures ε_{yy} of the sensor network for the load case n°14 (unit of measurement: [με]): (a) upper skin side view and (b) lower skin side view.

load case number 14, are reported in Fig. 26 and Fig. 27, derived from the experimental strain data previously shown in Fig. 24 and Fig. 25. The remarkable effectiveness of the SEA pre-extrapolation can be immediately appreciated: starting from a very limited number of measurement points, it generates a continuous strain field that faithfully represents even the regions not directly covered by sensors.

A preliminary sensitivity analysis on the SEA parameters confirmed that the contribution of β is negligible compared to α for the present case. Consistently with the literature [76], the best SEA performance in terms of displacement field reconstruction was achieved with β fixed to 10^{-6} and α in the range of 10^2–10^3 for both ε_{xx} and ε_{yy}. Within this range, the reconstructed displacement fields were sufficiently smooth while still following the input strain distribution across the entire domain. Tests with larger β values only produced mild over-smoothing and a slight increase in the error in points D_1 and D_2, while variations of α outside the indicated range did not significantly improve accuracy. These results indicate that the adopted parameter choice ensures a balanced trade-off between accuracy, stability, and computational cost.

Due to the symmetry of the sensor grid between the outer and inner sides of the stabilizer structure, the same α and β values were adopted for both sides.

Also, from both Fig. 26 and Fig. 27 it can be observed that the strain is influenced by the local shell thickness. The modification introduced in the methodology to account for thickness variations proved to be highly effective, leading to a more accurate reconstruction of the displacement and strain fields.

In addition, preliminary checks on the SEA mesh density showed that a coarser discretization tends to increase the reconstruction error due to loss of strain gradient resolution, while excessive refinement yields only marginal accuracy gains at a higher computational cost. The adopted

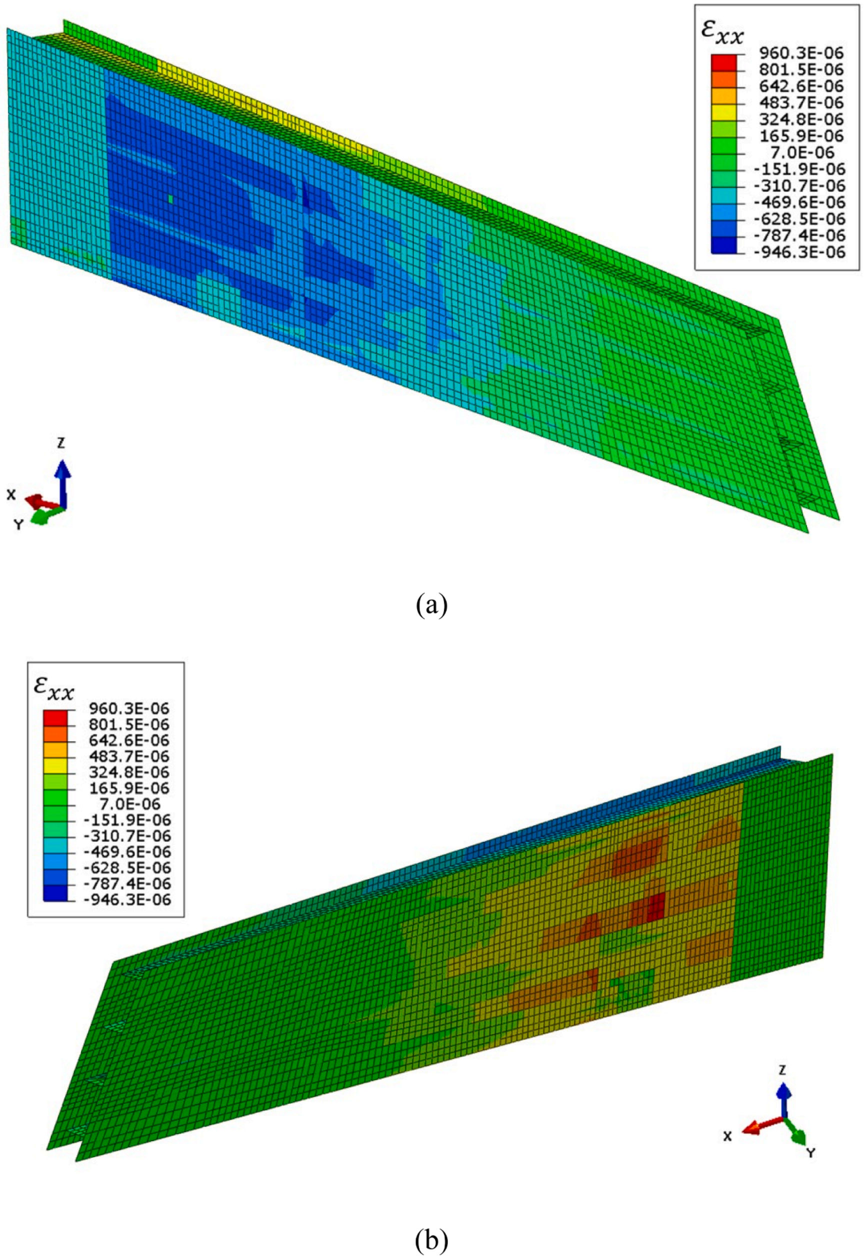

Fig. 26. Longitudinal input strain measures (after SEA pre-extrapolation) $\boldsymbol{\varepsilon_{xx}}$ of the sensor network for the load case n°14 (unit of measurement: [με]): (a) upper skin side view and (b) lower skin side view.

mesh therefore represents a balanced compromise, ensuring sufficient resolution of the strain field while keeping the procedure computationally efficient.

The SEA results obtained in the previous step were then used as input for the iFEM code to reconstruct the full displacement and strain fields, with the aim of comparing the displacements reconstructed by iFEM at locations D_1 and D_2 with the corresponding experimental measurements.

4.2. iFEM displacement reconstructions with ideal boundary conditions

The results for the U2 = UY displacement field of the stabilizer for load case number 14, obtained using the ideal boundary condition approach described in Section 3.3, are shown in Fig. 28 considering several views.

The general trend associated with the bending load is correctly captured by the iFEM reconstruction, which exhibits a qualitative pattern consistent with expectations. However, clear discrepancies are observed between the reconstructed $D_{1,iFEM,IBC}$ and $D_{2,iFEM,IBC}$ (IBC acronym for ideal boundary condition) and experimental measurements D_1 and D_2. As also reported in Table 5, for load case number 14 the experimental values are D_1 equal to 23.58 mm and D_2 equal to 22.26 mm, while the iFEM reconstruction under ideal boundary conditions yields $D_{1,iFEM,IBC}$ equal to 20.07 mm (−14.89 %) and $D_{2,iFEM,IBC}$ equal to 19.35 mm (−13.07 %), indicating a non-negligible underestimation of the actual displacements.

This underestimation is consistent with the subsequent analyses on boundary condition compliance: in this first phase, the assumption of ideal constraints (full clamp) results in the stabilizer being more confined, thereby exhibiting overall lower displacements.

The above considerations are further confirmed when examining the iFEM reconstructions for load case number 16 in Table 5. In this case, the loading condition is more complex to reconstruct, as it corresponds to a torsion-dominated scenario. The results, still expressed in terms of the

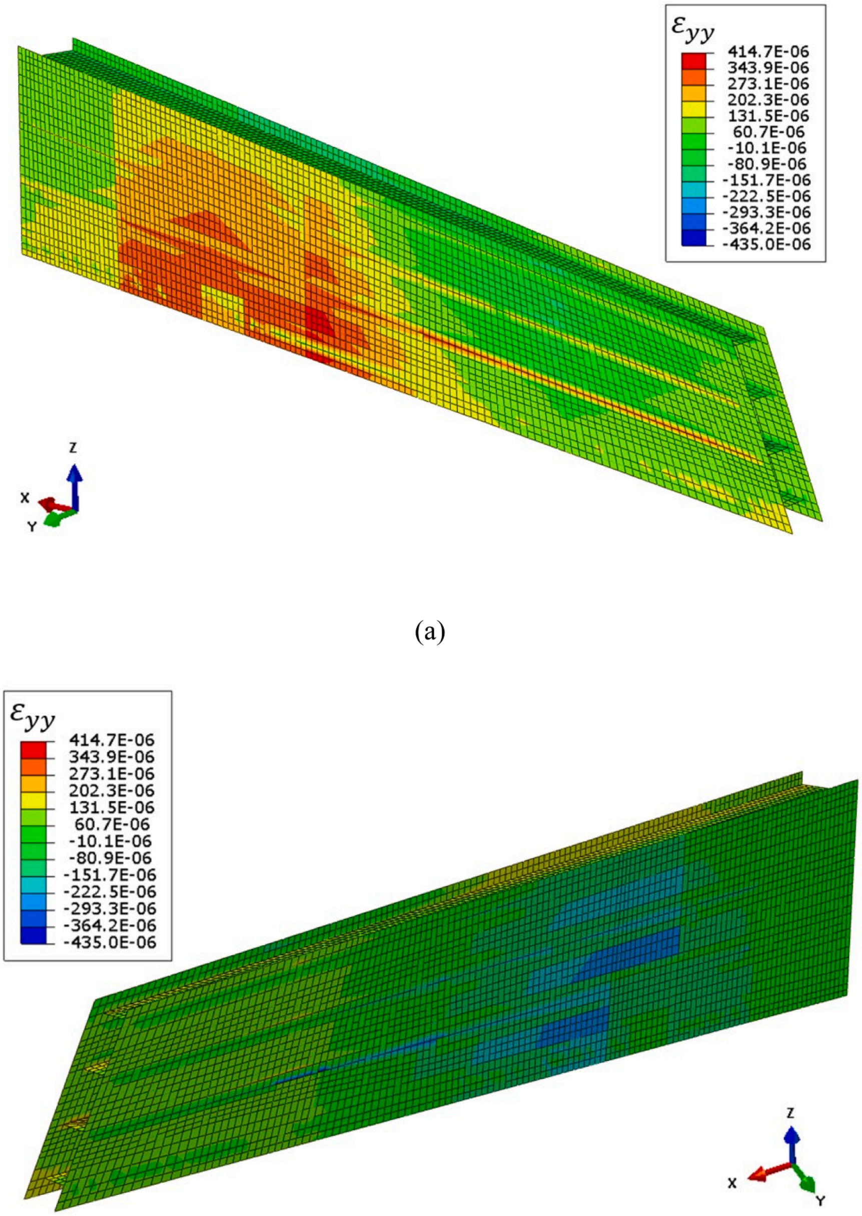

(a)

(b)

Fig. 27. Transversal input strain measures (after SEA pre-extrapolation) $\boldsymbol{\varepsilon_{yy}}$ of the sensor network for the load case n°14 (unit of measurement: [με]): (a) upper skin side view and (b) lower skin side view.

U2 displacement component, are presented in Fig. 29, providing additional insight into the reconstruction performance under a different and more challenging loading configuration.

The general trend associated with the torsional load is reasonably captured by reconstruction, which exhibits a qualitative pattern consistent with expectations. However, also in this case, non-acceptable discrepancies are observed between the reconstructed. In fact, for load case number 16 the experimental values are D_1 equal to 18.58 mm and D_2 equal to 12.96 mm, while the iFEM reconstruction under ideal boundary conditions yields $D_{1,iFEM,IBC}$ equal to 15.22 mm (−18.08 %) and $D_{2,iFEM,IBC}$ equal to 11.55 mm (−10.88 %).

Such observations made for both the bending and torsional cases are also evident in the other load scenarios reported in Table 5. Across all configurations, the percentage errors between the reconstructed displacements at the actuator locations and the corresponding experimental values do not fall below approximately 13 %. This level of discrepancy is generally considered unacceptable for advanced SHM applications, where accurate displacement reconstruction is essential to ensure reliable assessment of the structural state. For this reason, the next paragraph presents the results of the FE model of the support system, which enables the definition of more realistic boundary conditions for the stabilizer by explicitly modeling the non-ideal boundary conditions.

4.3. Internal action reconstruction and non-ideal boundary condition analysis

For simplicity, the discussion in this section focuses on the bending case only, namely load case 14. In addition to reconstructing the full displacement field, iFEM is also capable of reconstructing the strain field

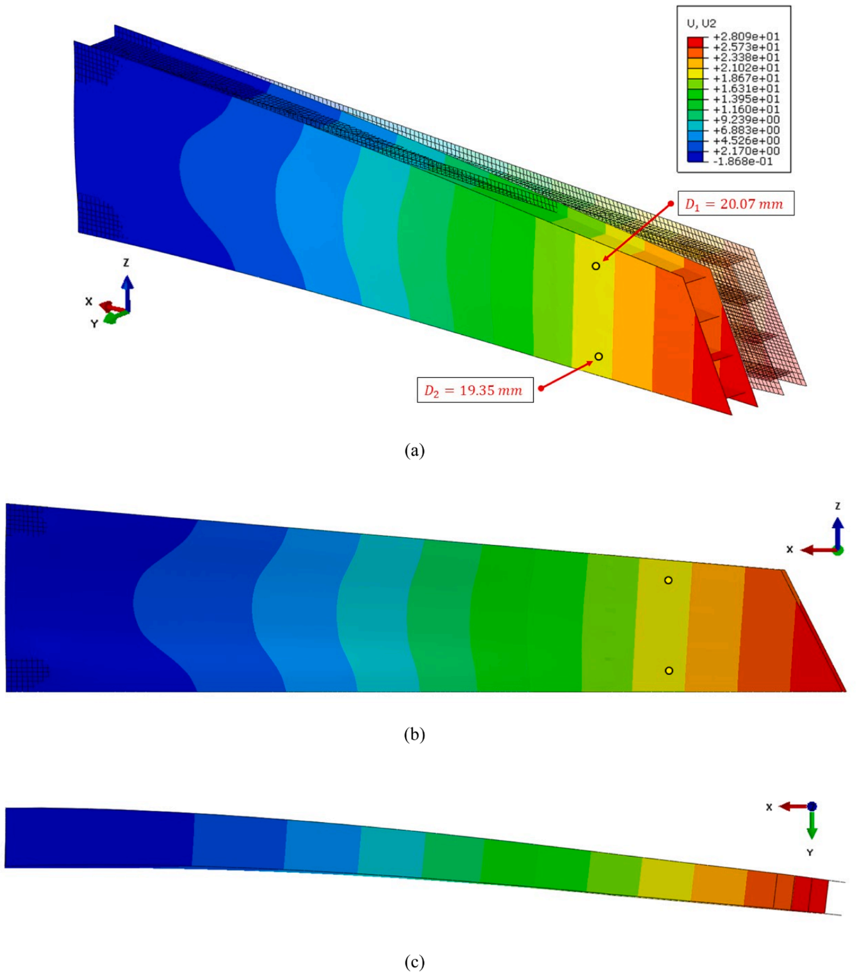

Fig. 28. Reconstruction results of the full field of vertical displacements U2 = UY for the load case n°14 (deformation scale factor = 10, displacement in [mm]) in the case of ideal boundary conditions: (a) 3D view with undeformed configuration, (b) 3D view and (c) top view.

Table 5
Comparison between experimental actuator displacement and iFEM reconstruction, including percentage error. $\boldsymbol{D}_{1,\boldsymbol{iFEM},\boldsymbol{IBC}}$ and $\boldsymbol{D}_{2,\boldsymbol{iFEM},\boldsymbol{IBC}}$ refers to the iFEM model with fully clamped (ideal) boundary conditions, while $\boldsymbol{D}_{1,\boldsymbol{iFEM},\mathrm{NIBC}}$ and $\boldsymbol{D}_{2,\boldsymbol{iFEM},\mathrm{NIBC}}$ refers to the iFEM model with non-ideal boundary conditions.

Load case	D_1 [*mm*]	D_2 [*mm*]	$D_{1,iFEM,IBC}$ [*mm*] and % error	$D_{2,iFEM,IBC}$ [*mm*] and % error	$D_{1,iFEM,NIBC}$ [*mm*] and % error	$D_{2,iFEM,NIBC}$ [*mm*] and % error
2	7.25	6.84	6.28 (−13.37 %)	5.88 (−14.04 %)	7.22 (−0.40 %)	6.71 (−1.88 %)
4	13.78	14.26	11.83 (−14.15 %)	12.36 (−13.31)	13.68 (−0.70 %)	14.20 (−0.45 %)
7	11.96	9.71	10.22 (−14.53 %)	8.57 (11.78 %)	11.89 (−0.56 %)	9.23 (−1.16 %)
8	15.25	14.66	12.99 (−17.89)	12.66 (−13.67)	15.23 (−0.14)	14.44 (−1.28 %)
10	22.10	21.80	18.54 (−16.10 %)	19.16 (−12.11 %)	22.04 (−0.27)	21.71 (−0.40)
14	23.58	22.26	20.07 (−14.89 %)	19.35 (−13.07 %)	23.51 (−0.30 %)	22.22 (−0.18 %)
16	18.58	12.96	15.22 (−18.08 %)	11.55 (−10.88 %)	18.49 (−0.48 %)	12.91 (−0.39 %)
20	32.52	30.28	28.29 (−13.00 %)	26.72 (−11.75 %)	32.91 (−1.19 %)	30.21 (−0.24 %)

and, through the methodology presented in Section 2.4, determining the internal actions at any desired cross-section of the stabilizer. An example of iFEM strain reconstruction for the load case 14 is reported in Fig. 30, for the ε_{xx} component only.

In the most general case, as shown in Fig. 23, six components of forces and moments (T_z, T_y, N, M_{fz}, M_{fy} and M_t) can be reconstructed for each cross-section of the stabilizer model. The results of these reconstructions, for the eight experimental cases analyzed, are reported in Table 6. As expected, for the bending-dominated cases the predominant contributions are T_y and M_{fz}, whereas for the torsion-dominated cases the most relevant internal actions are T_z and M_t. It should be noted that the internal action values presented above are to be regarded as

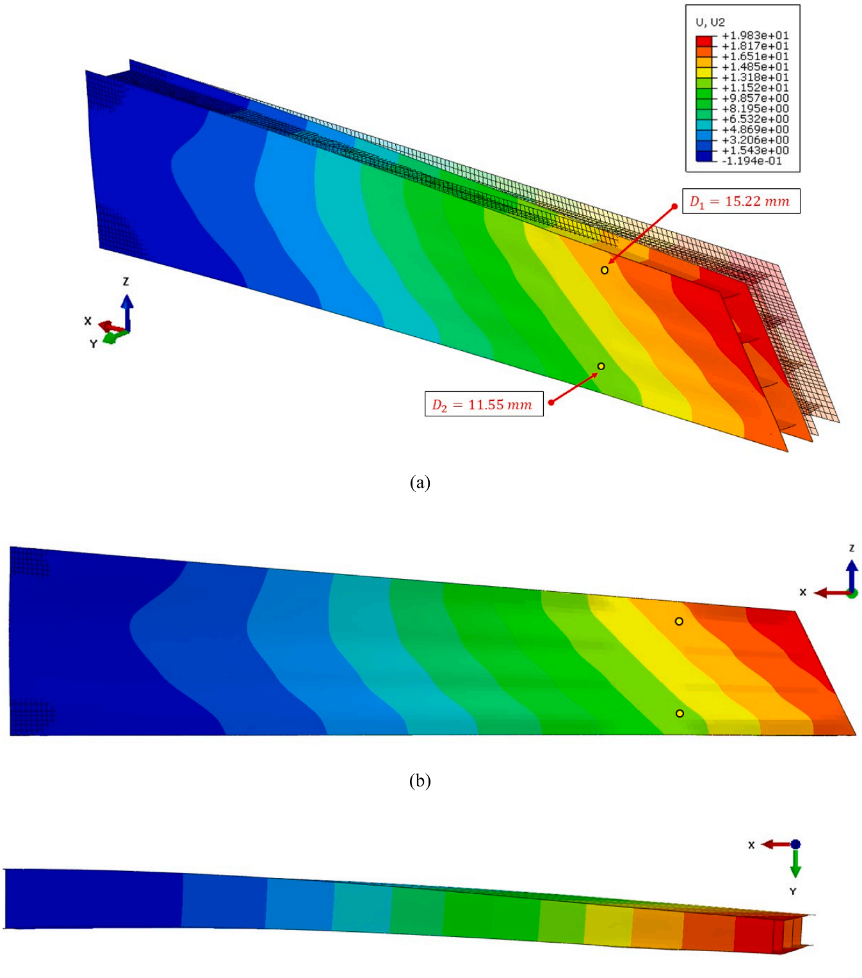

(a)

(b)

(c)

Fig. 29. Reconstruction results of the full field of vertical displacements U2 = UY for the load case n°16 (deformation scale factor = 10, displacement in [mm]) in the case of ideal boundary conditions: (a) 3D view with undeformed configuration, (b) 3D view and (c) top view.

estimates rather than exact values, as they were computed from strains (and thus displacements) reconstructed by iFEM in the previous case with ideal boundary conditions. Consequently, they are affected by a certain degree of error.

To further assess the reliability of the reconstruction, simplified consistency checks were performed. Considering, for simplicity, the load Case 2, the stabilizer can be assimilated to a cantilever beam subjected to two concentrated actuator loads. With two forces of about 2 kN each applied at a lever arm of approximately 2.7 m from the root, the expected bending moment at the clamped end is on the order of 10.8 kN·m, while the corresponding shear force is about 4.0 kN. The iFEM reconstruction yielded values of 10.3 kN·m for the bending moment and 3950 N for the shear force, showing very good agreement in order of magnitude (Table 6). This provides a useful plausibility check, even though no direct reference values were available.

The previously reconstructed internal actions are applied to the FE model of the support system, as described in Section 3.6. The results of this model, for load case 14, are shown in Fig. 31. This figure illustrates the magnitude displacement field of the support system under the loads transmitted by the stabilizer. As already discussed, the stand and the steel plate assembly are extremely stiff, and the only components exhibiting noticeable deformation are the brackets and their bolted connection to the steel plate. The displacements predicted by the FE model are on the order of approximately 1.8 mm—small in absolute terms but not negligible when aiming for accurate shape sensing of the stabilizer. As shown in the magnification of Fig. 31(b), the bending loads acting on the support system induce bracket deformations that are consistent with the nature and direction of the applied forces, confirming the structural response anticipated from the load transfer mechanism between the stabilizer and its support.

Based on these results, the displacement and rotation fields are extracted from the bracket surfaces interfacing with the stabilizer skins. These fields are then applied as non-ideal boundary conditions to a new iFEM model of the stabilizer, mapping properly the mesh nodes of the brackets to the ones of the stabilizer, thereby improving the representation of the constraints and, in turn, enhancing the reconstruction accuracy for both displacements and strains, with respect to the previous imposing of ideal full clamp.

4.4. iFEM displacement reconstructions with non-ideal boundary conditions

The displacement results obtained for load cases 14 and 16 using the non-ideal boundary condition procedure are presented in Fig. 32 and Fig. 33, respectively. Specifically, for the bending case, the experimental values are D_1 equal to 23.58 mm and D_2 equal to 22.26 mm, while the iFEM reconstruction under non-ideal boundary conditions (NIBC) yields $D_{1,iFEM,NIBC}$ equal to 23.51 mm (−0.30 %) and $D_{2,iFEM,NIBC}$ equal to 22.22 mm (−0.18 %), indicating a consistent higher accuracy with respect to the results presented in Section 4.2 (ideal boundary conditions).

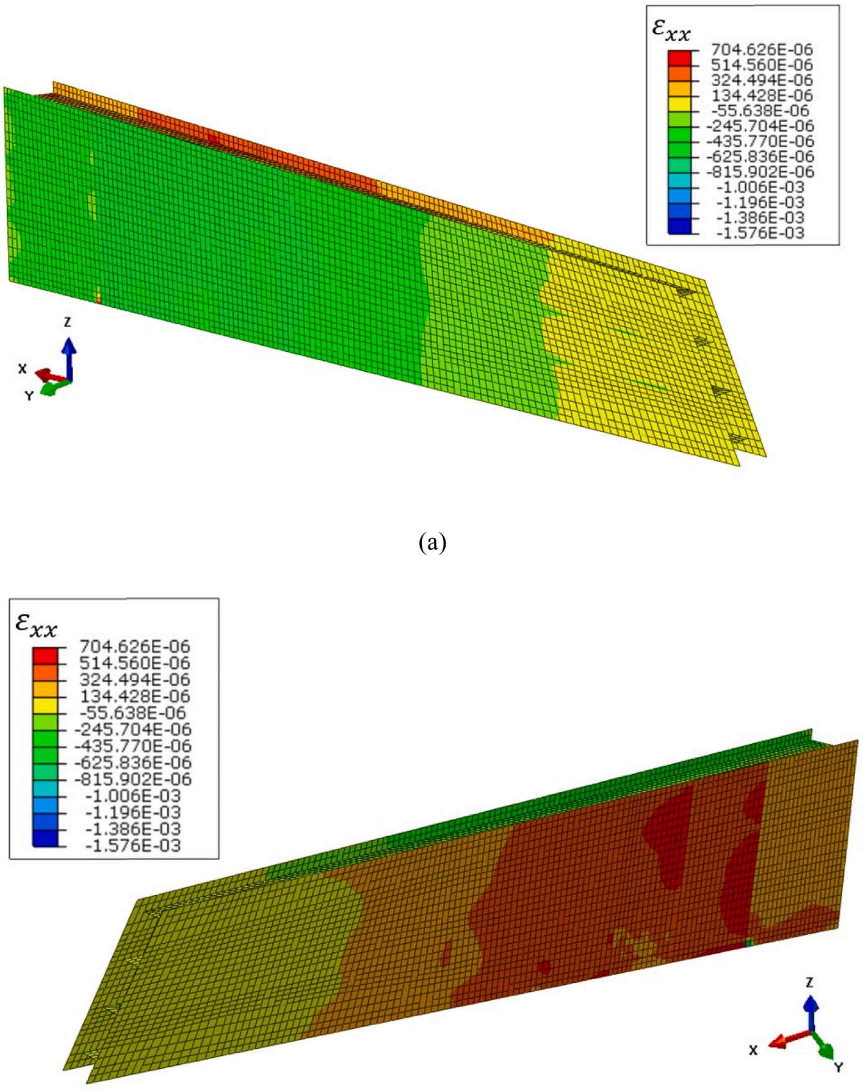

(a)

(b)

Fig. 30. Longitudinal reconstructed strain field $\boldsymbol{\varepsilon_{xx}}$ for the load case n°14 (unit of measurement: [με]): (a) upper skin side view and (b) lower skin side view.

Table 6
Internal action reconstruction at the root section of the stabilizer provided by the iFEM considering the reconstructed strain for all the scenarios studied in the present work.

Load case	$\lvert T_z \rvert$ [N]	$\lvert T_y \rvert [N]$	$\lvert N \rvert$ [N]	$\lvert M_{fz} \rvert$ [Nmm]	$\lvert M_{fy} \rvert$ [Nmm]	$\lvert M_t \rvert$ [Nmm]
2	341.35	3950	0	$10.3 \cdot 10^6$	$49.5 \cdot 10^4$	0
4		3899		$10.6 \cdot 10^6$		$56.5 \cdot 10^4$
7		1932		$10.7 \cdot 10^6$		$2.6 \cdot 10^4$
8		7956		$20.9 \cdot 10^6$		0
10		3993		$10.1 \cdot 10^6$		$112.3 \cdot 10^4$
14		11,912		$31.2 \cdot 10^6$		0
16		7782		$21.2 \cdot 10^6$		$2.20 \cdot 10^6$
20		15,832		$42.7 \cdot 10^6$		0

Furthermore, for the torsional case, the experimental values are D_1 equal to 18.58 mm and D_2 equal to 12.96 mm, while the iFEM reconstruction under ideal boundary conditions yields $D_{1,iFEM,NIBC}$ equal to 12.49 mm (−0.48 %) and $D_{2,iFEM,NIBC}$ equal to 12.91 mm (−0.39 %), also in this case much better than the ideal case.

Comparing Fig. 32 with Fig. 28 clearly highlights the impact of accounting for non-ideal boundary conditions. When the deformability of the brackets and their bolted connection to the steel plate is considered, small displacements and rotations are already present at the clamped section, enabling the reconstructed field to reach displacement values at the measurement points that closely match the experimental data. This improvement is consistently observed across all other cases studied, as reported in Table 5.

All the results presented here indicate that explicitly modeling the

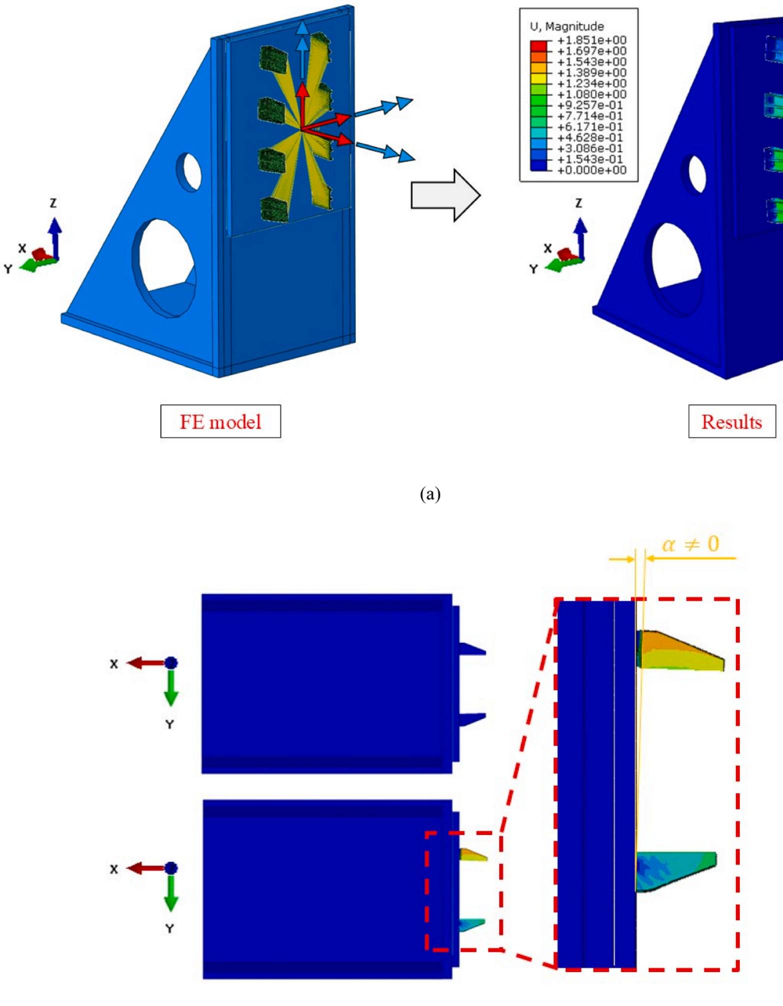

(a)

(b)

Fig. 31. Results obtained for the FE model of the support system: displacement magnitude (unit: mm) for load case No 14. (a) 3D view and (b) Magnification of the steel plate-brackets interface. Deformation scale factor = 5.

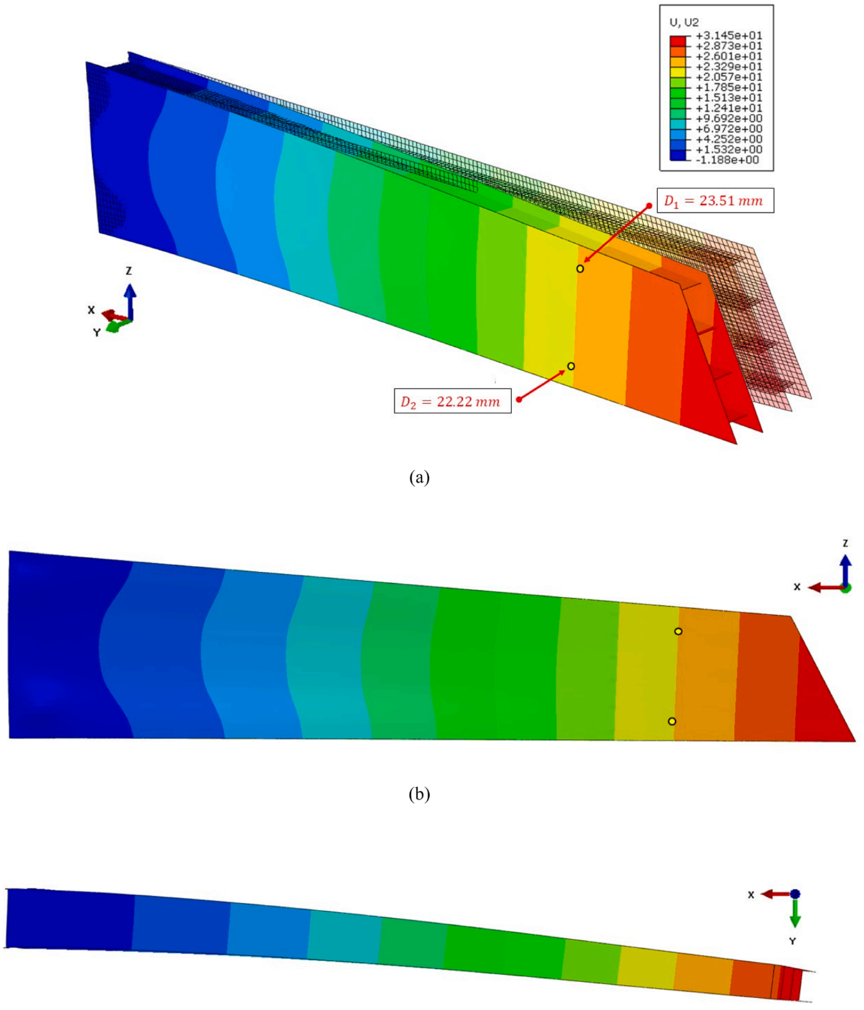

(a)

(b)

(c)

Fig. 32. Reconstruction results of the full field of vertical displacements U2 = UY for the load case n°14 (deformation scale factor = 10, displacement in [mm]) in the case of non-ideal boundary conditions: (a) 3D view with undeformed configuration, (b) 3D view and (c) top view.

non-ideal boundary conditions—by accounting for the actual compliance of the support system and its connections—significantly enhances the accuracy of iFEM-based reconstructions. By incorporating realistic displacement and rotation fields at the stabilizer–support interface, the method can more faithfully reproduce both the global deformation trends and the local displacement values at key measurement points, consistently reducing the discrepancies with experimental data across all load cases.

Importantly, including a static FE model of the support within the workflow does not limit the real-time applicability of the overall framework, as the support model can be precomputed and its influence incorporated into the boundary condition definition. This demonstrates the critical importance of accurately representing boundary conditions in shape-sensing applications, particularly in structural health monitoring contexts where precise displacement and strain reconstructions are essential for reliable damage detection and assessment.

Finally, the computational cost of the proposed workflow is very limited: the SEA pre-extrapolation requires <0.1 s per load case, while the iFEM reconstruction of the full stabilizer mesh is completed in about 1–2 s on a standard workstation (Intel® Core™ i9–14,900 K, 3.20 GHz, 128 GB RAM, CPU-only). This confirms that the SEA–iFEM chain operates within a few seconds, thereby supporting its feasibility for real-time or near real-time monitoring.

5. Concluding remarks

This work presented a comprehensive experimental–numerical framework for reconstructing the displacement, strain, and internal load fields in a full-scale composite UAV stabilizer, addressing key challenges related to sparse sensing, strain extrapolation, and boundary condition representation. The methodology combines Smoothing Element Analysis (SEA) to reconstruct continuous strain fields from a limited set of optical fiber measurements with the inverse Finite Element Method (iFEM) for full-field displacement and strain recovery.

A dedicated finite element model of the stabilizer support system was developed to explicitly represent non-ideal boundary conditions, including the compliance of brackets and bolted joints. This addition proved to be a crucial factor in improving reconstruction accuracy: for bending-dominated load cases, the displacement errors at key measurement points were reduced from values exceeding 14 % under the ideal boundary condition assumption to approximately 2–3 % when realistic constraints were applied. Comparable improvements were observed for torsional load cases, confirming the robustness of the approach across different loading scenarios.

The proposed framework also enables the estimation of internal force and moment distributions, offering valuable diagnostic insights beyond shape sensing. Importantly, the inclusion of the static FE model of the support system does not compromise the real-time applicability of the

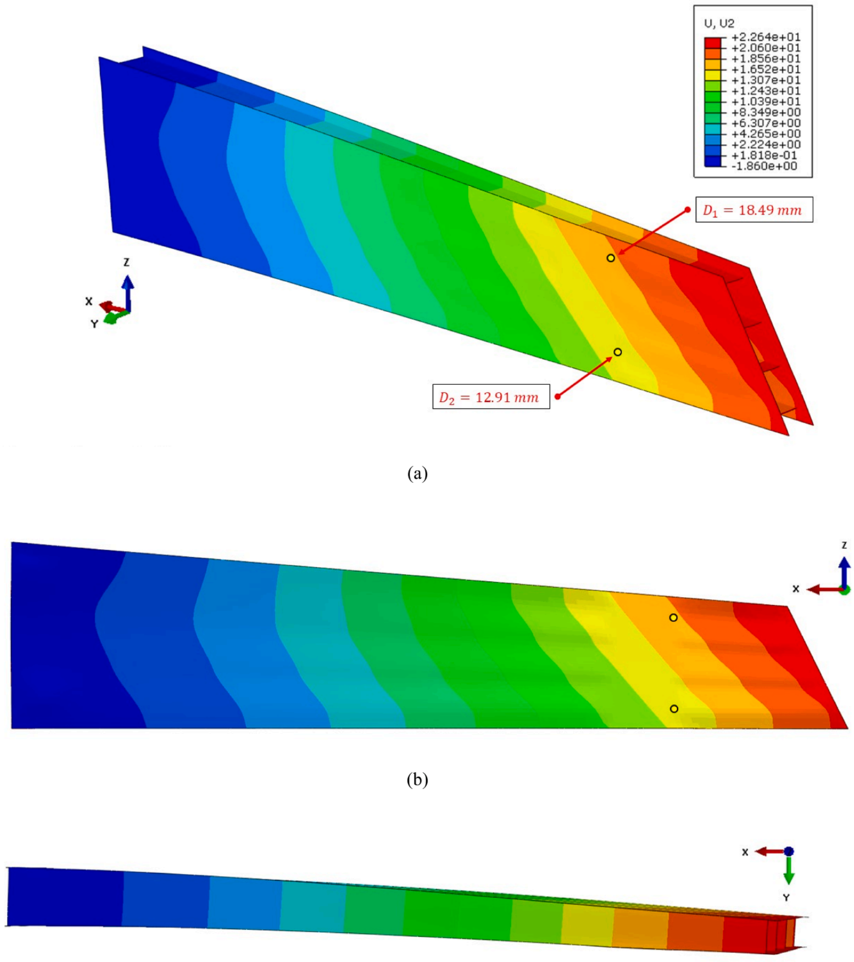

(a)

(b)

(c)

Fig. 33. Reconstruction results of the full field of vertical displacements U2 = UY for the load case n°16 (deformation scale factor = 10, displacement in [mm]) in the case of non-ideal boundary conditions: (a) 3D view with undeformed configuration, (b) 3D view and (c) top view.

method, as its effects on boundary conditions can be precomputed and integrated into the iFEM formulation.

The proposed boundary condition treatment already includes a data-driven correction, since the ideal BCs are refined using displacement information derived from actuator measurements and internal force transfer to the support. This represents a first step toward a data-driven calibration strategy. While this correction proved sufficient for the quasi-static cases considered here, future developments will focus on online calibration procedures, where boundary conditions can be adaptively updated in real time based on continuous sensor feedback.

Overall, the results demonstrate that accurate boundary modeling, coupled with advanced strain extrapolation techniques, is essential for achieving high-fidelity reconstructions in complex aerospace composite structures. This capability not only enhances the reliability of structural health monitoring but also supports future Digital Twin implementations for condition-based maintenance and operational decision-making.

CRediT authorship contribution statement

Jacopo Bardiani: Conceptualization, Methodology, Validation, Formal analysis, Investigation, Data curation, Writing – original draft, Writing – review & editing, Visualization. **Dario Poloni:** Conceptualization, Methodology, Visualization, Writing – review & editing. **Daniele Oboe:** Conceptualization, Methodology, Visualization, Writing – original draft. **Marco Giglio:** Resources, Methodology, Supervision, Project administration. **Andrea Manes:** Resources, Methodology, Supervision, Project administration, Writing – review & editing. **Claudio Sbarufatti:** Conceptualization, Methodology, Resources, Supervision, Project administration, Writing – review & editing.

Declaration of competing interest

The authors declare that they have no known competing financial interests or personal relationships that could have appeared to influence the work reported in this paper.

Data availability

The authors do not have permission to share data.

References

[1] D. Oboe, D. Poloni, C. Sbarufatti, M. Giglio, Towards automatic crack size estimation with iFEM for structural health monitoring, Sensors 23 (7) (2023) 3406, https://doi.org/10.3390/s23073406.

[2] J. Bardiani, C. Oppezzo, A. Manes, C. Sbarufatti, An inverse FEM for structural health monitoring of a containership: sensor network optimization for accurate displacement, strain, and internal force reconstruction, Sensors 25 (1) (2025) 276, https://doi.org/10.3390/s25010276.

[3] A. Deraemaeker, E. Reynders, G. De Roeck, J. Kullaa, Vibration-based structural health monitoring using output-only measurements under changing environment,

Mech. Syst. Signal. Process. 22 (2008) 34–56, https://doi.org/10.1016/j.ymssp.2007.07.004.

[4] C.R. Farrar, K. Worden, Structural Health Monitoring: A Machine Learning Perspective, John Wiley and Sons, Hoboken, NJ, USA, 2012. ISBN 9781119994336.

[5] F. Lambinet, Z.Sharif Khodaei, Measurement platform for structural health monitoring application of large-scale structures, Meas. J. Int. Meas. Confed. 190 (2022) 110675, https://doi.org/10.1016/j.measurement.2021.110675.

[6] A.H. Alavi, H. Hasni, P. Jiao, W. Borchani, N. Lajnef, Fatigue cracking detection in steel bridge girders through a self-powered sensing concept, J. Constr. Steel. Res. 128 (2017) 19–38, https://doi.org/10.1016/j.jcsr.2016.08.002.

[7] J. Warner, G. Bomarito, J. Hochhalter, W. Leser, P. Leser, J. Newman, A computationally-efficient probabilistic approach to model-based damage diagnosis, Int. J. Progn. Health Manage 8 (2017) 26, https://doi.org/10.36001/ijphm.2017.v8i2.2637.

[8] C. Sbarufatti, Optimization of an artificial neural network for fatigue damage identification using analysis of variance, Struct. Control Health Monit. 24 (2017) e1964, https://doi.org/10.1002/stc.1964.

[9] C. Sbarufatti, A. Manes, M. Giglio, Performance optimization of a diagnostic system based upon a simulated strain field for fatigue damage characterization, Mech. Syst. Signal. Process. 40 (2013) 667–690, https://doi.org/10.1016/j.ymssp.2013.06.003.

[10] D. Jones, C. Snider, A. Nassehi, J. Yon, B. Hicks, Characterising the digital twin: a systematic literature review, CIRP. J. Manuf. Sci. Technol. 29 (2020) 36–52, https://doi.org/10.1016/j.cirpj.2020.02.002.

[11] F. Tao, H. Zhang, A. Liu, A.Y.C. Nee, Digital twin in industry: state-of-the-art, IEEE Trans. Ind. Informatics 15 (2019) 2405–2415, https://doi.org/10.1109/TII.2018.2873186.

[12] D.J. Wagg, K. Worden, R.J. Barthorpe, P. Gardner, Digital twins: state-of-the-art and future directions for modeling and simulation in engineering dynamics applications, ASCE-ASME J. Risk Uncertain. Eng. Syst. Part B Mech. Eng. 6 (2020) 030901, https://doi.org/10.1115/1.4046739.

[13] F. Peng, L. Zheng, Y. Peng, C. Fang, X. Meng, Digital twin for rolling bearings: a review of current simulation and PHM techniques, Meas. J. Int. Meas. Confed. 201 (2022) 111728, https://doi.org/10.1016/j.measurement.2022.111728.

[14] E.H. Glaessgen, D.S. Stargel, The digital twin paradigm for future NASA and U.S. Air Force vehicles, in: Proceeding 53rd AIAA/ASME/ASCE/AHS/ASC Structures, Structural Dynamics and Materials Conference, Honolulu, HI, USA, 2012, pp. 1–14, https://doi.org/10.2514/6.2012-1818, 23–26 April.

[15] B.R. Seshadri, T. Krishnamurthy, Structural health management of damaged aircraft structures using the digital twin concept, in: Proceeding 25th AIAA/AHS Adaptive Structural. Conference, Grapevine, TX, USA, 2017, pp. 1–13, https://doi.org/10.2514/6.2017-1675, 9–13 January.

[16] B.T. Gockel, A.W. Tudor, M.D. Brandyberry, R.C. Penmetsa, E.J. Tuegel, Challenges with structural life forecasting using realistic mission profiles, in: Proc. 53rd AIAA/ASME/ASCE/AHS/ASC Structures, Structural Dynamics and Materials Conference, Honolulu, HI, USA, 2012, pp. 1–11, https://doi.org/10.2514/6.2012-1813, 23–26 April.

[17] E.J. Tuegel, A.R. Ingraffea, T.G. Eason, S.M. Spottswood, Reengineering aircraft structural life prediction using a digital twin, Int. J. Aerosp. Eng. 2011 (2011) 1–14, https://doi.org/10.1155/2011/154798.

[18] E.J. Tuegel, The airframe digital twin: some challenges to realization, in: Proceeding 53rd AIAA/ASME/ASCE/AHS/ASC Structures, Structural Dynamics and Materials Conference, Honolulu, HI, USA, 2012, pp. 1812–1820, https://doi.org/10.2514/6.2012-1812, 23–26 April.

[19] S.S. Johansen, A.R. Nejad, On digital twin condition monitoring approach for drivetrains in marine applications, Proc. Int. Conf. Offshore Mech. Arct. Eng. OMAE 10 (2019) 95152, https://doi.org/10.1115/omae2019-95152.

[20] T.G. Ritto, F.A. Rochinha, Digital twin, physics-based model, and machine learning applied to damage detection in structures, Mech. Syst. Signal. Process. 155 (2021) 107614, https://doi.org/10.1016/j.ymssp.2021.107614.

[21] F.K. Moghadam, A.R. Nejad, Online condition monitoring of floating wind turbines drivetrain by means of digital twin, Mech. Syst. Signal. Process. 162 (2022) 108087, https://doi.org/10.1016/j.ymssp.2021.108087.

[22] F. Tao, J. Cheng, Q. Qi, M. Zhang, H. Zhang, F. Sui, Digital twin-driven product design, manufacturing and service with big data, Int. J. Adv. Manuf. Technol. 94 (2018) 3563–3576, https://doi.org/10.1007/s00170-017-0233-1.

[23] W. Kritzinger, M. Karner, G. Traar, J. Henjes, W. Sihn, Digital twin in manufacturing: a categorical literature review and classification, IFAC-PapersOnLine 51 (2018) 1016–1022, https://doi.org/10.1016/j.ifacol.2018.08.474.

[24] G. Fedorko, V. Molnár, M. Vasiľ, R. Salai, Proposal of digital twin for testing and measuring of transport belts for pipe conveyors within the concept Industry 4.0, Meas, J. Int. Meas. Confed. 174 (2021) 108978, https://doi.org/10.1016/j.measurement.2021.108978.

[25] M. Wang, S. Feng, A. Incecik, G. Królczyk, Z. Li, Structural fatigue life prediction considering model uncertainties through a novel digital twin-driven approach, Comput. Methods Appl. Mech. Eng. 391 (2022) 114512, https://doi.org/10.1016/j.cma.2021.114512.

[26] J. Bardiani, A. Manes, M. Giglio, C. Sbarufatti, Shape sensing and damage identification with iFEM on a double bottom structure of a containership, in: F. Concli, L. Maccioni, R. Vidoni, D.T. Matt (Eds.), Latest Advancements in Mechanical Engineering. ISIEA 2024, Lecture Notes in Networks and Systems, vol. 1124, Springer, Cham, 2024, https://doi.org/10.1007/978-3-031-70462-8_22.

[27] A. Kefal, I. Emami, M. Yildiz, A. Tessler, A smoothed iFEM approach for efficient shape-sensing applications: numerical and experimental validation on composite structures, Mech. Syst. Signal. Process. 152 (2021) 107486, https://doi.org/10.1016/j.ymssp.2020.107486.

[28] A. Tessler, J.L. Spangler, A variational principle for reconstruction of elastic deformations in shear deformable plates and shells. NASA/TM-2003-212445, National Aeronautics and Space Administration, Langley Research Center, 2003.

[29] A. Tessler, J. Spangler, Inverse FEM for full-field reconstruction of elastic deformations in shear deformable plates and shells, in: Proceedings of 2nd European Workshop on Structural Health Monitoring, 2004, 10.1.1.81.6767.

[30] M. Gherlone, P. Cerracchio, M. Mattone, M. Di Sciuva, A. Tessler, Shape sensing of 3D frame structures using an inverse finite element method, Int. J. Solids. Struct. 49 (2012) 3100–3112, https://doi.org/10.1016/j.ijsolstr.2012.06.009.

[31] Y. Zhao, J. Du, H. Bao, Q. Xu, Optimal sensor placement based on eigenvalues analysis for sensing deformation of wing frame using iFEM, Sensors 18 (2018) 2424, https://doi.org/10.3390/s18082424.

[32] M. Gherlone, P. Cerracchio, M. Mattone, M. Di Sciuva, A. Tessler, An inverse finite element method for beam shape sensing: theoretical framework and experimental validation, Smart. Mater. Struct. 23 (2014) 045027, https://doi.org/10.1088/0964-1726/23/4/045027.

[33] K. Chen, K. Cao, G. Gao, H. Bao, Shape sensing of Timoshenko beam subjected to complex multi-node loads using isogeometric analysis, Meas. J. Int. Meas. Confed. 184 (2021) 109958, https://doi.org/10.1016/j.measurement.2021.109958.

[34] J. Wang, L. Ren, R. You, T. Jiang, Z. Jia, G. Wang, Experimental study of pipeline deformation monitoring using the inverse finite element method based on the IBeam3 element, Meas. J. Int. Meas. Confed. 184 (2021) 109881, https://doi.org/10.1016/j.measurement.2021.109881.

[35] F. Zhao, L. Xu, H. Bao, J. Du, Shape sensing of variable cross-section beam using the inverse finite element method and isogeometric analysis, Meas. J. Int. Meas. Confed. 158 (2020) 107656, https://doi.org/10.1016/j.measurement.2020.107656.

[36] R. You, L. Ren, An enhanced inverse beam element for shape estimation of beam-like structures, Meas. J. Int. Meas. Confed. 181 (2021) 109575, https://doi.org/10.1016/j.measurement.2021.109575.

[37] D. Poloni, M. Morgese, C. Wang, T. Taylor, M. Giglio, F. Ansari, C. Sbarufatti, Reference-free distributed monitoring of deflections in multi-span bridges, Eng. Struct. 323 (2025) 119277, https://doi.org/10.1016/j.engstruct.2024.119277.

[38] A. Kefal, E. Oterkus, Displacement and stress monitoring of a chemical tanker based on inverse finite element method, Ocean Eng. 112 (2016) 33–46, https://doi.org/10.1016/j.oceaneng.2015.11.032.

[39] A. Kefal, E. Oterkus, Displacement and stress monitoring of a Panamax containership using inverse finite element method, Ocean Eng. 119 (2016) 16–29, https://doi.org/10.1016/j.oceaneng.2016.04.025.

[40] M. Li, A. Kefal, B.C. Cerik, E. Oterkus, Dent damage identification in stiffened cylindrical structures using inverse finite element method, Ocean Eng. 198 (2020) 106944, https://doi.org/10.1016/j.oceaneng.2020.106944.

[41] A. Kefal, E. Oterkus, A. Tessler, J.L. Spangler, A quadrilateral inverse-shell element with drilling degrees of freedom for shape sensing and structural health monitoring, Eng. Sci. Technol. Int. J. 19 (2016) 1299–1313, https://doi.org/10.1016/j.jestch.2016.03.006.

[42] A. Tessler, J.L. Spangler, A least-squares variational method for full-field reconstruction of elastic deformations in shear-deformable plates and shells, Comput. Methods Appl. Mech. Eng. 194 (2005) 327–339, https://doi.org/10.1016/j.cma.2004.03.015.

[43] D. Oboe, L. Colombo, C. Sbarufatti, M. Giglio, Shape sensing of a complex aeronautical structure with inverse finite element method, Sensors 21 (2021) 342–351, https://doi.org/10.3390/s21041388.

[44] S. Niu, Y. Zhao, H. Bao, Shape sensing of plate structures through coupling inverse finite element method and scaled boundary element analysis, Meas. J. Int. Meas. Confed. 190 (2022) 110676, https://doi.org/10.1016/j.measurement.2021.110676.

[45] F. Zhao, H. Bao, An improved inverse finite element method for shape sensing using isogeometric analysis, Meas. J. Int. Meas. Confed. 167 (2021) 108282, https://doi.org/10.1016/j.measurement.2020.108282.

[46] M. Esposito, A novel shape sensing approach based on the coupling of modal virtual sensor expansion and iFEM: numerical and experimental assessment on composite stiffened structures, Comput. Struct. 305 (2024) 107520, https://doi.org/10.1016/j.compstruc.2024.107520.

[47] V. Biscotti, R. Roy, M. Gherlone, Shape monitoring of morphing wing structures using the inverse finite element method, Comput. Struct. 309 (2025) 107652, https://doi.org/10.1016/j.compstruc.2025.107652.

[48] P. Cerracchio, M. Gherlone, A. Tessler, Real-time displacement monitoring of a composite stiffened panel subjected to mechanical and thermal loads, Meccanica 50 (2015) 2487–2496, https://doi.org/10.1007/s11012-015-0146-8.

[49] U. Papa, S. Russo, A. Lamboglia, G. Del Core, G. Iannuzzo, Health structure monitoring for the design of an innovative UAS fixed wing through inverse finite element method (iFEM), Aerosp. Sci. Technol. 69 (2017) 439–448, https://doi.org/10.1016/j.ast.2017.07.005.

[50] L. Colombo, C. Sbarufatti, M. Giglio, Definition of a load adaptive baseline by inverse finite element method for structural damage identification, Mech. Syst. Signal. Process. 120 (2019) 584–607, https://doi.org/10.1016/j.ymssp.2018.10.041.

[51] M. Li, A. Kefal, E. Oterkus, S. Oterkus, Structural health monitoring of an offshore wind turbine tower using iFEM methodology, Ocean Eng. 204 (2020) 107291, https://doi.org/10.1016/j.oceaneng.2020.107291.

[52] A. Kefal, An efficient curved inverse-shell element for shape sensing and structural health monitoring of cylindrical marine structures, Ocean Eng. 188 (2019) 106262, https://doi.org/10.1016/j.oceaneng.2019.106262.

[53] M.A. Abdollahzadeh, A. Kefal, M. Yildiz, A comparative and review study on shape and stress sensing of flat/curved shell geometries using C^0-continuous family of iFEM elements, Sensors 20 (2020) 3808, https://doi.org/10.3390/s20143808.

[54] A. Kefal, J.B. Mayang, E. Oterkus, M. Yildiz, Three-dimensional shape and stress monitoring of bulk carriers based on iFEM methodology, Ocean Eng. 147 (2018) 256–267, https://doi.org/10.1016/j.oceaneng.2017.10.040.

[55] M. Esposito, M. Gherlone, Composite wing box deformed-shape reconstruction based on measured strains: optimization and comparison of existing approaches, Aerosp. Sci. Technol. 99 (2020) 105758, https://doi.org/10.1016/j.ast.2020.105758.

[56] M. Esposito, M. Gherlone, P. Marzocca, External loads identification and shape sensing on an aluminum wing box: an integrated approach, Aerosp. Sci. Technol. 114 (2021) 106743, https://doi.org/10.1016/j.ast.2021.106743.

[57] P. Cerracchio, M. Gherlone, M. Di Sciuva, A. Tessler, A novel approach for displacement and stress monitoring of sandwich structures based on the inverse finite element method, Compos. Struct. 127 (2015) 69–76, https://doi.org/10.1016/j.compstruct.2015.02.081.

[58] A. Kefal, A. Tessler, E. Oterkus, An enhanced inverse finite element method for displacement and stress monitoring of multilayered composite and sandwich structures, Compos. Struct. 179 (2017) 514–540, https://doi.org/10.1016/j.compstruct.2017.07.078.

[59] F. Zhao, H. Bao, J. Liu, K. Li, Shape sensing of multilayered composite and sandwich beams based on refined zigzag theory and inverse finite element method, Compos. Struct. 261 (2021) 113321, https://doi.org/10.1016/j.compstruct.2020.113321.

[60] A. Kefal, I.E. Tabrizi, M. Tansan, E. Kisa, M. Yildiz, An experimental implementation of inverse finite element method for real-time shape and strain sensing of composite and sandwich structures, Compos. Struct. 258 (2021) 113431, https://doi.org/10.1016/j.compstruct.2020.113431.

[61] L. Colombo, D. Oboe, C. Sbarufatti, F. Cadini, S. Russo, M. Giglio, Shape sensing and damage identification with iFEM on a composite structure subjected to impact damage and non-trivial boundary conditions, Mech. Syst. Signal. Process. 148 (2021) 107163, https://doi.org/10.1016/j.ymssp.2020.107163.

[62] D. Oboe, L. Colombo, C. Sbarufatti, M. Giglio, Comparison of strain pre-extrapolation techniques for shape and strain sensing by iFEM of a composite plate subjected to compression buckling, Compos. Struct. 262 (2021) 113587, https://doi.org/10.1016/j.compstruct.2021.113587.

[63] F. Ganjdoust, A. Kefal, A. Tessler, A novel delamination damage detection strategy based on inverse finite element method for structural health monitoring of composite structures, Mech. Syst. Signal. Process. 192 (2023) 110202, https://doi.org/10.1016/j.ymssp.2023.110202.

[64] R. Roy, M. Gherlone, Delamination and skin-spar debond detection in composite structures using the inverse finite element method, Materials. (Basel) 16 (5) (2023) 1969, https://doi.org/10.3390/ma16051969.

[65] A. Kefal, C. Diyaroglu, M. Yildiz, E. Oterkus, Coupling of peridynamics and inverse finite element method for shape sensing and crack propagation monitoring of plate structures, Comput. Methods Appl. Mech. Eng. 391 (2022) 114520, https://doi.org/10.1016/j.cma.2021.114520.

[66] T. Li, M. Cao, J. Li, L. Yang, H. Xu, Z. Wu, Structural damage identification based on integrated utilization of inverse finite element method and pseudo-excitation approach, Sensors 21 (2021) 606, https://doi.org/10.3390/s21020606.

[67] A. Tessler, H.R. Riggs, S.C. Macy, A variational method for finite element stress recovery and error estimation, Comput. Methods Appl. Mech. Eng. 111 (1994) 369–382, https://doi.org/10.1016/0045-7825(94)90140-6.

[68] A. Tessler, T.J.R. Hughes, A three-node Mindlin plate element with improved transverse shear, Comput. Methods Appl. Mech. Eng. 50 (1985) 71–101, https://doi.org/10.1016/0045-7825(85)90114-8.

[69] A. Tessler, H.R. Riggs, C.E. Freese, G.M. Cook, An improved variational method for finite element stress recovery and a posteriori error estimation, Comput. Methods Appl. Mech. Eng. 155 (1998) 15–30, https://doi.org/10.1016/S0045-7825(97)00135-7.

[70] H.R. Riggs, A. Tessler, H. Chu, C^1-continuous stress recovery in finite element analysis, Comput. Methods Appl. Mech. Eng. 143 (1997) 299–316, https://doi.org/10.1016/S0045-7825(96)01151-6.

[71] D. Oboe, C. Sbarufatti, M. Giglio, Physics-based strain pre-extrapolation technique for inverse finite element method, Mech. Syst. Signal. Process. 177 (2022) 109167, https://doi.org/10.1016/j.ymssp.2022.109167.

[72] J. Bardiani, R. Faure Ragani, L. Pinello, A. Kefal, A. Manes, C. Sbarufatti, Shape sensing and damage detection of composite pressure vessels using inverse finite element method coupled with physics-based strain pre-extrapolation, Thin-Walled Struct. (2025) 123569. In press.

[73] D. Poloni, D. Oboe, C. Sbarufatti, M. Giglio, Towards a stochastic inverse finite element method: a Gaussian process strain extrapolation, Mech. Syst. Signal. Process. 189 (2023) 110056, https://doi.org/10.1016/j.ymssp.2022.110056.

[74] M. Li, Z. Wu, H. Yang, H. Huang, Direct damage index based on inverse finite element method for structural damage identification, Ocean Eng. 221 (2021) 108545, https://doi.org/10.1016/j.oceaneng.2020.108545.

[75] M. Li, Z. Wu, D. Jia, S. Qiu, W. He, Structural damage identification using strain mode differences by the iFEM based on the convolutional neural network (CNN), Mech. Syst. Signal. Process. 165 (2022) 108289, https://doi.org/10.1016/j.ymssp.2021.108289.

[76] D. Poloni, D. Oboe, C. Sbarufatti, M. Giglio, Variable thickness strain pre-extrapolation for the inverse finite element method, Sensors 23 (2023) 1733, https://doi.org/10.3390/s23031733.

[77] Z. Zhang, Z. Lu, Y. Yang, L. Dong, S.N. Atluri, Framework of physically consistent homogenization and multiscale modeling of shell structures, AIAA J. (2024) 1–14, https://doi.org/10.2514/1.J064645.

[78] V. Chamola, P. Kotesh, A. Agarwal, N. Gupta, M. Guizani, A comprehensive review of unmanned aerial vehicle attacks and neutralization techniques, Ad. Hoc. Netw. 111 (2021) 102324, https://doi.org/10.1016/j.adhoc.2020.102324.

[79] MTS, "MTS DuraGlide™ 244 hydraulic actuators datasheet," 2017.

[80] M. Smith, ABAQUS/Standard User's Manual, Version 6.9, Dassault Systèmes Simulia Corp, United States, 2009.